Trajectory Tracking Wide-Area Control for Power Systems

Ryan Thomas Elliott

A dissertation
submitted in partial fulfillment of the
requirements for the degree of

Doctor of Philosophy

University of Washington

2020

Reading Committee:

Daniel Kirschen, Chair

Payman Arabshahi, Chair

Baosen Zhang

Program Authorized to Offer Degree:
Electrical and Computer Engineering

University of Washington

Abstract

Trajectory Tracking Wide-Area Control for Power Systems

Ryan Thomas Elliott

Co-Chairs of the Supervisory Committee:
Donald W. and Ruth Mary Close Professor Daniel Kirschen
Electrical and Computer Engineering

Associate Professor Payman Arabshahi
Electrical and Computer Engineering

This dissertation reassesses traditional approaches to power system stabilization in the context of contemporary measurement and communication technology. Changes in bulk system dynamics driven by increases in power electronically-coupled generation and load pose challenges to existing control strategies. Rather than attempting to maintain a static equilibrium, we explore strategies that drive the system toward a desired trajectory. This approach emerges from a time-varying linearization of the equations of motion for a synchronous machine. First, we develop and demonstrate a generalized power system stabilizer architecture that incorporates local information with a real-time estimate of the speed of the center of inertia. This estimate is synthesized from data collected over wide-area measurement systems. We then turn our attention toward a new method for stabilizing transient disturbances by modulating the active power injected by inverter-based resources. The response of each inverter is calculated to drive the local bus voltage angle toward a trajectory that tracks the angle of the center of inertia. The results of this endeavor indicate that trajectory tracking control can improve both transient and small-signal stability, while also increasing tuning flexibility. In particular, we show that it is possible to decouple the effect of the control action on inter-area and local modes of oscillation from the effect on the frequency regulation mode.

TABLE OF CONTENTS

LIST OF FIGURES

LIST OF TABLES

GLOSSARY

AUTOMATIC VOLTAGE REGULATOR: a component of the excitation system of a synchronous machine that regulates terminal voltage, or a related compensated voltage, by modulating the field current.

CENTER OF INERTIA: a weighted-average of power system dynamic states, such as rotor speed or angle, where the weights are the inertia constants of the synchronous machines (analogous to the center of mass).

CO-SIMULATION: a computing paradigm in which two or more software platforms or models are coupled to permit all relevant processes and dynamics to be simulated together.

DIRECT METHODS: a class of methods for power system stability analysis that do not require the solution of the differential equations that describe the system's dynamics, *i.e.*, simulated trajectories.

EQUAL-AREA CRITERION: a graphical method for determining transient stability in two-machine systems or single-machine infinite bus frameworks.

ENERGY STORAGE SYSTEM: in the examples discussed herein, an inverter-based resource with the ability to store energy and inject or withdraw active power from the bulk transmission system.

FIRST SWING: the initial extreme value, *i.e.*, local minimum or maximum, attained by the rotor angle deviation of a synchronous machine following a transient (severe) disturbance.

FREQUENCY REGULATION MODE: a very low-frequency power system mode, typically below 0.1 Hz, in which the rotor speeds of all synchronous generation units participate.

HIERARCHICAL ENGINE FOR LARGE-SCALE INFRASTRUCTURE CO-SIMULATION: a state-of-the-art co-simulation platform developed by a multi-laboratory research effort through the U.S. Department of Energy's Grid Modernization Lab Consortium.

HYBRID METHODS: a class of methods for determining power system stability that use energy function analysis to examine the results of time-domain simulation.

INVERTER-BASED RESOURCE: in the examples discussed herein, a power electronically coupled device with the ability to inject active power into the bulk transmission system.

LINEAR TIME-VARYING SYSTEMS: systems with linear dynamics that evolve with time, often arising from the linearization of a nonlinear system about a trajectory.

LOW-VOLTAGE POWER LOGIC: a scheme for imposing voltage-dependent bounds on the current that may be injected into a power system by an inverter-based resource.

MINIWECC: a reduced-order dynamic model of the North American Western Interconnection designed to facilitate time-domain simulation and dynamic analysis.

NETWORK SIMULATOR 3: a discrete-event network simulator for modeling Internet-Protocol-based communication systems.

NORTH AMERICAN WESTERN INTERCONNECTION: the power system interconnection spanning the western United States; British Columbia and Alberta, Canada; and the northern part of the Baja California, Mexico.

PHASOR MEASUREMENT UNIT: a time-synchronized sensing device capable of measuring the magnitude and angle of electrical phasors.

POWER SYSTEM STABILIZER: a control system designed to damp generator rotor oscillations by creating a component of the electrical torque that is in phase with deviations in rotor speed.

POWER SYSTEM TOOLBOX: a MATLAB-based software library that facilitates time-domain simulation of nonlinear systems, numerical linearization, and modal analysis.

REAL-TIME CONTROL: a control paradigm that utilizes data communicated over a low-latency network to automatically control power system resources.

REMEDIAL ACTION SCHEME: an action (or sequence thereof) that is triggered when a particular power system condition or event is detected, such as underfrequency load shedding.

SYSTEM PROTECTION SCHEME: see REMEDIAL ACTION SCHEME.

TRAJECTORY-TRACKING CONTROL: a class of control techniques in which the system states are driven toward a desired trajectory rather than a static point in the state space.

USER DATAGRAM PROTOCOL: a connectionless, message-oriented transport layer protocol that is part of the Internet protocol suite.

WIDE-AREA MEASUREMENT SYSTEM: a network of time-synchronized sensors, typically with sub-second sampling capability, distributed across a large geographical region.

ACRONYMS

AVR: automatic voltage regulator

ESS: energy storage system

FACTS: flexible ac transmission system

HELICS: hierarchical engine for large-scale infrastructure co-simulation

HVDC: high-voltage direct current

IBR: inverter-based resource

NS-3: Network Simulator 3

IP: Internet Protocol

LTI: linear time-invariant

LTV: linear time-varying

LVPL: low-voltage power logic

PMU: phasor measurement unit

PSS: power system stabilizer

PST: Power System Toolbox for MATLAB

RAS: remedial action scheme

UDP: User Datagram Protocol

WAMS: wide-area measurement system

WECC: Western Electric Coordinating Council

ACKNOWLEDGMENTS

It has been a privilege to pursue a Ph.D. in the Renewable Energy Analysis Lab (REAL) at the University of Washington. I am inspired every day by my colleagues and professors, without whom this work would not have been possible. I have many people to thank, both at UW and beyond. Due to space constraints this section is not exhaustive, and any omissions are purely unintentional. First, I would like to thank my doctoral advisors Daniel Kirschen and Payman Arabshahi. I sincerely appreciate you providing me with the latitude to pursue the research directions that I felt drawn toward. Had Professor Kirschen not joined the department while I was working on my master's degree, I may never have embarked on a career in research. Professor Arabshahi was an equal partner, and I will be forever grateful for his perspective, insight, and good humor.

I would be remiss not to mention the numerous other UW professors who played a role in shaping my thought process. Much of my power systems background is attributable to the teaching of Rich Christie and Mark Damborg. The tools I reach for on a daily basis were honed in their courses. The other formative force in my early education was Mohamed El-Sharkawi, who is sadly no longer with us. He set an example of how to conduct oneself not only as an engineer, but also as a person. The department has been fortunate to recruit talented young professors to carry on the tradition of excellence in power systems at UW. Thank you to Baosen Zhang and Brian Johnson for serving on my committee, and for upholding such a high standard of research quality. Of the professors not chiefly focused on power systems, this work owes the most to Sam Burden. His teaching heavily influenced my understanding and interpretation of linear time-varying systems. I would also like to thank Miguel Ortega-Vasquez for many stimulating discussions on engineering and beyond.

During my Ph.D. studies, I was fortunate to be the recipient of several fellowships. From the Clean Energy Institute, I would like to thank Dan Schwartz, David Ginger, and Shaun Taylor. From the Washington Clean Energy Testbeds, I would like to thank Mike Pomfret and Phil Cox. Being a CEI Fellow was a tremendous opportunity to grow outside of my own discipline, and to learn how to talk about my work to a broad audience. The first and last year of my studies were funded by the Grainger Foundation. I greatly appreciate their financial assistance and recognition of my academic performance. Thank you to Mehran Mesbahi for providing valuable feedback during my General Exam. And thank you to Mani Vadari for his generosity and for taking the time to share lunch with us at the UW Club.

On the long journey of doing a Ph.D., I frequently drew strength and inspiration from my UW colleagues. I would like to thank Ahlmahz Negash, Yury Dvorkin, Hrvoje Pandžić, Yishen Wang, Zeyu Wang, Ting Qiu, and Tsz-Kin (Marco) Au. During my master's studies, they showed me what a rewarding experience being a graduate student could be. Thank you to Kelly Kozdras and Ricardo Fernández-Blanco for being such thoughtful collaborators throughout our work on sharing energy storage. Thank you to Yuanyuan Shi for helping me pass Professor Fazel's course on convex optimization, and to Atinuke Ademola-Idowu for venturing into the world of power system dynamics with me. Thank you to Yao Long and Chanaka Keerthisinghe for being the best office mates imaginable. There are too many people from this period to mention everyone individually, but I am continually impressed by the talented and kind engineers attracted to study in our lab.

Joining Sandia National Laboratories after finishing my master's degree was a turning point in my career, and my life. If my résumé had not landed on the desk of César Silva-Monroy, I may never have moved to Albuquerque to pursue a career in research. My deepest gratitude for helping me get acclimated to a new city, a new job, and for showing me that it was possible to be a first-rate researcher while living a fulfilling life outside of work. I will be forever grateful to Ross Guttromson for giving me an opportunity as a junior engineer to

work on a slate of interesting and important projects. Thank you to Ray Byrne and Dave Schoenwald for your mentorship, and for being patient with me as I learned the ropes. Thank you to Abe Ellis for inviting me to participate in the WECC Renewable Energy Modeling Task Force (REMTF). Thank you to Jason Neely for your candor and sense of humor. And thank you to Brian Pierre, Ricky Concepcion, Felipe Wilches-Bernal, and Matt Reno for carrying the torch while I was away.

In addition to my Sandia colleagues, I have been blessed to work with a number of extraordinary collaborators over the years. Of those, I would particularly like to thank Dan Trudnowski from Montana Tech. He is largely responsible for sparking my interest in power system dynamics and controls. His honest feedback helped me accelerate my development as researcher. I would also like to thank Matt Donnelly, R.J. Hallett, James Colwell, and Samuel Ojetola. Of the projects that I have worked on, I especially cherish my years spent studying and developing the Pacific DC Intertie wide-area damping control system. From the Bonneville Power Administration, I would like to thank Dmitry Kosterev, Steve Yang, Tony Faris, Greg Stults, Jeff Barton, and Hamody Hindi. From the WECC REMTF, I would like to thank Pouyan Pourbeik, Juan Sanchez-Gasca, Jamie Weber, Jay Senthil, and all participants that I had the pleasure of getting to know. I learned a tremendous amount about power system dynamics and modeling from each of you.

Lastly, and most importantly, I would like to thank my family. To my Mom, Priscilla, for reminding me that on a scale from 1–10, it's a 2. To my Dad, Tom, for saving all of my schoolwork since I was in kindergarten. To my stepdad, Martin, for geeking out over 8-track tapes and all things EE with me. To my sister, LeAnne, for not sleeping on the roof after I was born. To my brother-in-law, Casey, for treating me like family since I was 14. To my brother, Sam, for always reminding me what's important in life. And to my grandparents, whom I hope I've made proud.

DEDICATION

For my parents

Chapter 1

INTRODUCTION

Skate to where the puck is going, not where it has been.

– Walter Gretzky, *advice to his young son*

Driven primarily by increases in power electronically-coupled generation and load, electric grids are losing inertia, voltage support, and oscillation damping. Simultaneously, the system load is becoming stiffer with respect to changes in voltage [34, 55]. Advancements in wide-area measurement technology have made it possible to implement control strategies that act on information transmitted over long distances in nearly real time [40, 51, 58, 60]. In this work, we reassess traditional approaches to power system stabilization beginning with synchronous machine power system stabilizers (PSS). We then turn our attention to a new method for stabilizing transient disturbances. These approaches work in tandem with the first controller designed to produce supplemental damping torque, and the latter synchronizing torque.

In [64], Vittal defines stability as, "that property which ensures that the system will remain in operating equilibrium through the normal and abnormal operating conditions." In the context of rotor angle stability, there are two classes of abnormal operating conditions that are of particular interest: *small-signal* disturbances where the system response is well-described by a linearized model, and *transient* (or severe) disturbances where a nonlinear model is required [35]. These distinctions inform the way power systems engineers think, and the solutions they design for maintaining stability.

1.1 The Motivation for Trajectory Tracking Controls

The primary function of PSSs is to improve oscillation damping, and thereby support small-signal stability [9, 15, 22, 36]. Conventional speed-based PSSs rely upon a constant reference. During transient disturbances, in which the system frequency often drifts from its nominal value, this static reference may have unintended consequences. Specifically, it creates the potential for PSSs to degrade transient stability by counteracting the voltage signal sent to the exciter by the automatic voltage regulator (AVR) [15]. In Chapter 2, we present a new type of PSS that mitigates this limitation. The trajectory tracking approach we develop provides increased flexibility for balancing the transient and small-signal aspects of the control response.

The solution space for stabilizing transient disturbances is primarily composed of voltage regulation, protection, and remedial action schemes (RAS) [3, 8, 73, 78]. The concept of bolstering transient stability via active power modulation has garnered some attention in the literature but is not yet widespread in practice [31]. As the penetration of inverter-based resources (IBRs) increases, we expect this approach to become more common. In Chapter 3, we present a new method for stabilizing transient disturbances by modulating the active power injected by IBRs, such as utility-scale energy storage systems. This method is built upon a similar theoretical framework as the PSS architecture developed in Chapter 2.

Power system control strategies usually stem from time-invariant linearizations of the system dynamics. Hence, they aim to hold the system at a static point in the state space. The chief drawbacks of such control schemes are:

- The linearized models on which these schemes are based lose accuracy as the system operating point migrates away from the static equilibrium. This limits their utility during severe disturbances and complicates the task of designing controls for transient stability.

- They provide limited tuning flexibility because current multi-band compensation tech-

niques are based upon linear filtering. This increases the difficulty of decoupling the control response associated with the frequency regulation mode from the rest of the system dynamics.

- They may degrade the voltage response by interfering with other regulating components due to lack of coordination.

In this work, we develop control strategies for driving the system toward a desired trajectory that varies with time. We focus on strategies that are enabled by wide-area measurement systems (WAMS). For our applications, trajectory tracking control strategies must satisfy the following requirements:

- The nonequilibrium (or desired) trajectory must be selected sensibly so that the control action supports the navigation of the system operating point from one equilibrium to another.

- They must be fully implementable given local information and/or the data that is typically accessible over contemporary wide-area measurement systems.

- They must be designed to function safely and correctly with realistic communication and measurement systems. In practice these systems possess various delays, sources of noise, and other non-idealities (*e.g.*, jitter, dropouts).

- They shall not degrade the voltage response or interfere with the coordination between the PSS and AVR in synchronous machines.

1.2 Overview of Trajectory Tracking

In broad terms, a trajectory is a collection of dynamic system variables that evolve as a function of time. More specifically, a trajectory represents a state-input pair of the form $\{\overline{x}(t), \overline{u}(t)\}$, where $\overline{x}(t) \in \mathbb{R}^n$ is the value of the state trajectory at time t and $\overline{u}(t) \in \mathbb{R}^m$

the corresponding input. The basic idea behind trajectory tracking is that rather than attempting to drive the system toward a static equilibrium (or other fixed point in the state space), the system is directed toward a desired trajectory. As shown in Chapters 2 and 3, control strategies of this type follow from time-varying linearizations of nonlinear systems. In such cases, the trajectory around which the system is linearized becomes the trajectory that the system is driven toward by the control. Hence, selecting the nonequilibrium trajectory appropriately is of the utmost importance. In this work, we explore the implications of basing the nonequilibrium trajectory on the motion of the center of inertia of the power system.

Recall that the center of inertia is a weighted average of power system dynamic states, usually rotor speed or angle, in which the inertia constants of the synchronous machines serve as the weights [57]. This concept is analogous to the center of mass in systems that exhibit translational (or linear) motion. Basing the nonequilibrium trajectory on the center of inertia has many useful properties, chief among them that it promotes synchronism during transient disturbances. To estimate the speed and/or angle of the center of inertia in nearly real time, we utilize simulated WAMS data.

1.3 Scope of the Work

The objectives of this research endeavor are to:

- Improve the damping of electromechanical modes of oscillation, both inter-area and local in nature.

- To the extent possible, reduce overshoot in the step response and minimize the frequency nadir following transient disturbances.

- Prevent loss of synchronism following large disturbances such as faults, line outages, and generator trips.

- Increase line ratings on stability-limited transmission corridors by improving utilization of existing thermal capacity.

Chapter 2

A GENERALIZED PSS ARCHITECTURE FOR BALANCING TRANSIENT AND SMALL-SIGNAL RESPONSE

For decades, power system stabilizers paired with high initial response automatic voltage regulators have served as an effective means of meeting sometimes conflicting system stability requirements. Driven primarily by increases in power electronically-coupled generation and load, the dynamics of large-scale power systems are rapidly changing. Electric grids are losing inertia and traditional sources of voltage support and oscillation damping. The system load is becoming stiffer with respect to changes in voltage. In parallel, advancements in wide-area measurement technology have made it possible to implement control strategies that act on information transmitted over long distances in nearly real time. In this chapter, we present a power system stabilizer architecture that can be viewed as a generalization of the standard $\Delta\omega$-type stabilizer. The control strategy utilizes a real-time estimate of the center-of-inertia speed derived from wide-area measurements. This approach creates a flexible set of trade-offs between transient and small-signal response, making synchronous generators better able to adapt to changes in system dynamics. The phenomena of interest are examined using a two-area test case and a reduced-order model of the North American Western Interconnection. To validate the key findings under realistic conditions, we employ a state-of-the-art co-simulation platform to combine high-fidelity power system and communication network models. The benefits of the proposed control strategy are retained even under pessimistic assumptions of communication network performance.

2.1 Motivation

The delicate balance between synchronizing and damping torque components in a synchronous machine creates a conflicting set of stability-oriented exciter performance requirements [13, 14, 21, 35]. Power system stabilizers (PSS) have long played a critical role in satisfying these requirements; however, changes in bulk system dynamics pose challenges to existing control strategies. As inverter-coupled variable generation displaces synchronous machines, electric grids lose inertia and traditional sources of voltage support and oscillation damping. Correspondingly, the rapid growth of power electronic loads may make the system load stiffer with respect to changes in voltage [34, 55]. In parallel with these changes, wide-area measurement systems (WAMS) have transformed power system monitoring. The deployment of phasor measurement units (PMUs) has made it is possible to implement control strategies that act on information transmitted over long distances in nearly real time [40, 51, 58, 60]. Despite the proliferation of inverter-coupled resources, it is projected that synchronous generation will account for a significant fraction of the capacity of large-scale power systems for decades to come [62]. As the dynamics of these systems change, it may become necessary to rethink how synchronous machines are controlled.

In this chapter, we derive a new PSS architecture that can be viewed as a generalization of the standard $\Delta\omega$-type stabilizer. This control strategy stems from a time-varying linearization of the equations of motion for a synchronous machine. It utilizes a real-time estimate of the center-of-inertia speed derived from a set of wide-area measurements. The proposed strategy improves the damping of both local and inter-area modes of oscillation. The ability of the stabilizer to improve damping is decoupled from its role in shaping the system response to transient disturbances. Consequently, the interaction between the PSS and automatic voltage regulator (AVR) can be fine-tuned based on voltage requirements. This approach creates a flexible set of trade-offs between transient and small-signal response, making synchronous generators better able to adapt to changes in system dynamics. Analysis and simulation show that this strategy is tolerant of communication delay, traffic congestion, and jitter.

2.1.1 Literature Review

The role that PSSs play in shaping the dynamic system response to severe transient disturbances, such as generator trips, is explored in [9, 15, 22, 36]. In [15], Dudgeon *et al.* show that the actions of PSSs and AVRs are dynamically interlinked. High initial response AVRs support transient stability but can reduce the damping of electromechanical modes of oscillation. The primary function of PSSs is to improve oscillation damping, but they can also degrade transient stability by counteracting the voltage signal sent to the exciter by the AVR. Managing these interactions through coordinated AVR and PSS design is studied in [16, 37, 52]. In [22], Grondin, Kamwa *et al.* present a multi-band PSS compensator aimed at improving transient stability by adding damping to the lowest natural resonant frequency. The objectives of this compensation approach are similar to those we outline in Section 2.2. We present a PSS architecture that features a new type of multi-band compensator that leverages wide-area measurements to achieve amplitude response attenuation.

Employing remote, or global, input signals to improve the performance of power system damping controllers has inspired many research efforts including [4, 11, 29, 32, 71, 76]. In [4], Aboul-Ela *et al.* propose a PSS architecture with two inputs, a local signal used mainly for damping the local mode and a global signal for damping inter-area modes. For the global signal, [4] considers tie-line active power flows and speed difference signals that provide observability of specific inter-area modes. As stated in [22], the ideal stabilizing signal for a PSS "should be in phase with the deviation of the generator speed from the average speed of the entire system." To approximate this ideal signal, the rotor speed is typically passed through a washout (highpass) filter, which may insufficiently attenuate steady-state changes in rotor speed and/or introduce excess phase lead into the bottom end of the control band. In contrast, we explore the implications of combining local measurements with a real-time estimate of the center-of-inertia speed.

The research community is actively working to develop simulation techniques for studying the impact of communication networks on power systems. *Federated co-simulation envi-*

ronments consist of two or more independent simulation platforms combined so that they exchange data and software execution commands. In [26], Hopkinson *et al.* present EPOCHS, a co-simulation environment that combined Network Simulator 2 (ns-2) with PSLF and PSCAD/EMTDC. Many subsequent research efforts followed, including [12, 39, 49]. In this thesis, the Hierarchical Engine for Large-scale Infrastructure Co-Simulation (HELICS) is employed [49]. We use this state-of-the-art framework to federate a communication network model developed in ns-3 with a power system model developed in the MATLAB-based Power System Toolbox (PST).

2.1.2 Chapter Organization

The remainder of this chapter is organized as follows. Section 2.2 derives a generalization of the standard $\Delta\omega$-type PSS enabled by wide-area measurements. The impact of this control strategy on a two-area test system is examined in Section 2.3. Section 2.4 evaluates how the main results scale to large systems using a reduced-order model of the North American Western Interconnection. In Section 2.4.3, we study the effect of nonideal communication network performance using co-simulation. Section 2.5 summarizes and concludes.

2.2 Proposed Method

The proposed PSS architecture arises from a time-varying linearization of the equations of motion for a synchronous machine. Here we briefly restate some key concepts and definitions from the theory of continuous-time linear time-varying systems. In the control strategy derivation, these concepts will be applied to the nonlinear form of the swing equation.

2.2.1 Linear Time-Varying Systems

Let $f : \mathbb{R}^n \times \mathbb{R}^m \to \mathbb{R}^n$ denote a nonlinear vector field

$$\dot{x}(t) = f(x(t), u(t)), \tag{2.1}$$

where $x(t) \in \mathbb{R}^n$ is the system state at time t and $u(t) \in \mathbb{R}^m$ the input. Recall that a time-varying linearization of f takes the form

$$\Delta\dot{x}(t) = A(t)\Delta x(t) + B(t)\Delta u(t), \tag{2.2}$$

where $\Delta x(t) = x(t) - \overline{x}(t)$ and $\Delta u(t) = u(t) - \overline{u}(t)$. The time-varying trajectory about which the system is linearized is determined by $\overline{x}(t)$ and $\overline{u}(t)$.

The state-space matrices can be expressed compactly as

$$A(t) = D_x f(\overline{x}(t), \overline{u}(t)) \tag{2.3}$$

$$B(t) = D_u f(\overline{x}(t), \overline{u}(t)), \tag{2.4}$$

where the operator D_x returns the Jacobian matrix of partial derivatives with respect to x evaluated at time t, and D_u returns the analogous matrix of partials with respect to u. In general, the state-space representation is time-varying when $\overline{x}(t)$ and $\overline{u}(t)$ define a nonequilibrium trajectory.

2.2.2 Control Strategy Derivation

This derivation applies the concepts introduced in Section 2.2.1 to the equations of motion for a synchronous machine. Stating the nonlinear swing equation in terms of the per-unit

accelerating power, we have

$$\dot{\omega}(t) = -\frac{D}{2H}[\omega(t) - \omega_0] + \frac{1}{2H\omega(t)}[P_m(t) - P_e(t)], \tag{2.5}$$

where ω_0 is the per-unit synchronous speed, D the damping coefficient, and H the inertia constant [21, 35]. Linearizing (2.5) about a nonequilibrium trajectory yields

$$\begin{aligned}\Delta\dot{\omega}(t) = &-\left[\frac{D}{2H} + \frac{\overline{P}_m(t) - \overline{P}_e(t)}{2H\overline{\omega}(t)^2}\right]\Delta\omega(t) \\ &+ \frac{1}{2H\overline{\omega}(t)}[\Delta P_m(t) - \Delta P_e(t)],\end{aligned} \tag{2.6}$$

where $\Delta\omega(t) = \omega(t) - \overline{\omega}(t)$, $\Delta P_m(t) = P_m(t) - \overline{P}_m(t)$, and $\Delta P_e(t) = P_e(t) - \overline{P}_e(t)$.

A new damping coefficient arises from analysis of (2.6)

$$\mathfrak{D}(t) = D + \frac{\overline{P}_m(t) - \overline{P}_e(t)}{\overline{\omega}(t)^2}. \tag{2.7}$$

Using this coefficient, (2.6) can be restated as

$$\Delta\dot{\omega}(t) = -\frac{\mathfrak{D}(t)}{2H}\Delta\omega(t) + \frac{1}{2H\overline{\omega}(t)}[\Delta P_m(t) - \Delta P_e(t)]. \tag{2.8}$$

Hence, as with a standard $\Delta\omega$-type stabilizer it is possible to add damping in the LTV reference frame by creating a component of electrical torque that is in phase with the rotor speed deviations. The difference is that the speed deviations are defined such that $\Delta\omega(t) = \omega(t) - \overline{\omega}(t)$, where $\overline{\omega}(t)$ is a function of time that tracks changes in the overall system operating point. The time-varying reference $\overline{\omega}(t)$ makes it possible to almost completely wash out steady-state changes in rotor speed from the control error.

2.2.3 Nonequilibrium Speed Trajectory

In this thesis, we will examine the implications of treating $\overline{\omega}(t)$ as a real-time estimate of the center-of-inertia speed

$$\overline{\omega}(t) \approx \frac{\sum_{i\in\mathcal{I}} H_i\omega_i(t)}{\sum_{i\in\mathcal{I}} H_i}, \tag{2.9}$$

where i is the unit index and $\mathcal{I}$ the set of all online conventional generators. The right-hand side of (2.9) corresponds to the classical center-of-inertia definition, dating back to at least [57].

A related quantity that incorporates the machine apparent power ratings is studied in [61]. This alternative approach may be more effective than (2.9) in capturing the discrepancy in size between large and small machines with similar inertia constants.

The question of how to compute $\overline{\omega}(t)$ for real-time control applications is an interesting research problem in itself that is mostly outside the scope of this chapter. A promising method is presented in [46]. At the time of this writing, rotor speed measurements are seldom available through wide-area measurement systems; however, a straightforward way of estimating (2.9) would be a weighted average of frequency measurements

$$\overline{\omega}(t) = \frac{1}{f_0} \sum_{k \in \mathcal{K}} \alpha_k f_k(t), \tag{2.10}$$

where k is the sensor index, and f_0 the nominal system frequency. The frequency signal reported by the kth sensor is denoted by $f_k(t)$, and the associated weight by α_k. The weights are nonnegative and sum to one, *i.e.*, $1^T \alpha = 1$. For simplicity, we will consider the arithmetic mean in which $\alpha_k = 1/|\mathcal{K}|$ for all k, where $|\mathcal{K}|$ denotes the cardinality of $\mathcal{K}$ or simply the number of available sensors. The research contributions presented in this chapter do not depend strongly on this choice. There are numerous implementation-related issues posed by any wide-area control scheme, such as how to handle missing or corrupted data. For examples of how these problems may be addressed, see [50, 51].

2.2.4 A Generalization of the $\Delta\omega$-Type PSS

The control strategy implied by (2.8) can be generalized to encompass the standard $\Delta\omega$-type PSS. Splitting the linear time-invariant (LTI) control error $\Delta\omega(t) = \omega_i(t) - \omega_0$ into two constituent parts and taking the linear combination yields

$$\Delta\nu(t) \triangleq \beta_1[\omega_i(t) - \overline{\omega}(t)] + \beta_2[\overline{\omega}(t) - \omega_0], \tag{2.11}$$

where β_1 and β_2 are independent tuning parameters restricted to the unit interval. In Section 2.4, we show how the open-loop frequency response between the input to the exciter and the output of the PSS can be shaped by adjusting these parameters. The first term

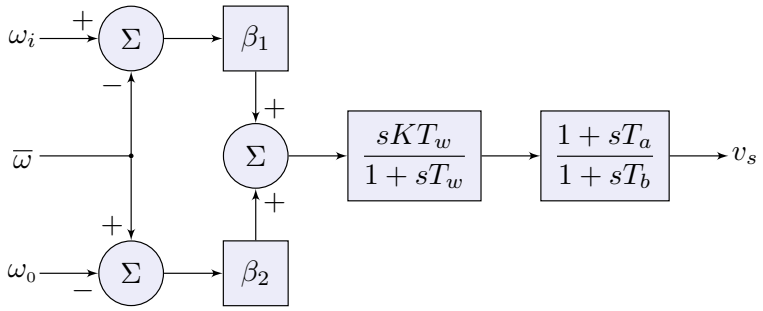

Figure 2.1: Generalized $\Delta\omega$-type PSS block diagram.

in (2.11) follows directly from (2.8), and the second makes it possible to implement a standard $\Delta\omega$-type PSS using the same framework. As in Section 2.2.3, $\overline{\omega}(t)$ is a real-time estimate of the center-of-inertia speed. Figure 2.1 shows the block diagram corresponding to this control strategy where v_s is the output of the PSS. If necessary, more than one lead-lag compensation stage may be employed.

The *frequency regulation mode* of a power system is a very low-frequency mode, typically below 0.1 Hz, in which the rotor speeds of all synchronous generation units participate [22, 67]. As a consequence of synchronism, the shape of this mode is such that all conventional generators are in phase with one another. As its name implies, the frequency regulation mode is sensitive to load composition, turbine governor time constants, and droop gains. When $\beta_1 > \beta_2$, the control tuning prioritizes the damping of inter-area and local modes of oscillation while de-emphasizing the frequency regulation mode. The converse is true when $\beta_1 < \beta_2$. In the special case that $\beta_1 = \beta_2$, we have a conventional $\Delta\omega$-type PSS. The resulting control error in this case is exactly the same as in the standard formulation presented in [35]. Table 2.1 summarizes the effect of β_1 and β_2 on the PSS tuning.

The diagram shown in Figure 2.1 accurately illustrates the control strategy; however, the structure can be clarified further. Expanding the second term in (2.11) gives

$$\Delta\nu(t) = \beta_1[\omega_i(t) - \overline{\omega}(t)] + \beta_2\overline{\omega}(t) - \beta_2\omega_0. \tag{2.12}$$

Table 2.1: Effect of Control Parameters on PSS Tuning

Parameter Values	Tuning Description
$\beta_1 > \beta_2$	Targets inter-area and local modes
$\beta_1 < \beta_2$	Targets the frequency regulation mode
$\beta_1 = \beta_2 \neq 0$	Standard $\Delta\omega$-type PSS
$\beta_1 = \beta_2 = 0$	No PSS control

Thus, we can construct the control error in (2.11) with a constant reference and a single feedback signal

$$\Delta\nu(t) = \nu(t) - \nu_{\text{ref}}, \text{ where} \tag{2.13}$$

$$\nu_{\text{ref}} = \beta_2\omega_0, \text{ and} \tag{2.14}$$

$$\nu(t) = \beta_1[\omega_i(t) - \overline{\omega}(t)] + \beta_2\overline{\omega}(t). \tag{2.15}$$

The results described in this chapter are based on the strategy defined by (2.13)–(2.15) and illustrated in Figure 2.1.

For the sake of completeness, we present a further refinement that permits the per-unit synchronous speed ω_0 to serve as the reference. The basic idea is to divide (2.12) by β_2, taking care to account for the case where $\beta_2 = 0$. Beginning with the control error, we have

$$\Delta\widetilde{\omega}(t) \triangleq \widetilde{\omega}(t) - \omega_0. \tag{2.16}$$

The feedback signal $\widetilde{\omega}(t)$ is then given by

$$\widetilde{\omega}(t) = \begin{cases} (\beta_1/\beta_2)[\omega_i(t) - \overline{\omega}(t)] + \overline{\omega}(t), & \text{for } \beta_2 > 0 \\ \beta_1[\omega_i(t) - \overline{\omega}(t)] + \omega_0, & \text{for } \beta_2 = 0. \end{cases} \tag{2.17}$$

This construction is similar to a conventional $\Delta\omega$-type stabilizer where the local speed measurement $\omega_i(t)$ has been replaced by $\widetilde{\omega}(t)$. Further illustrating this connection, when β_1

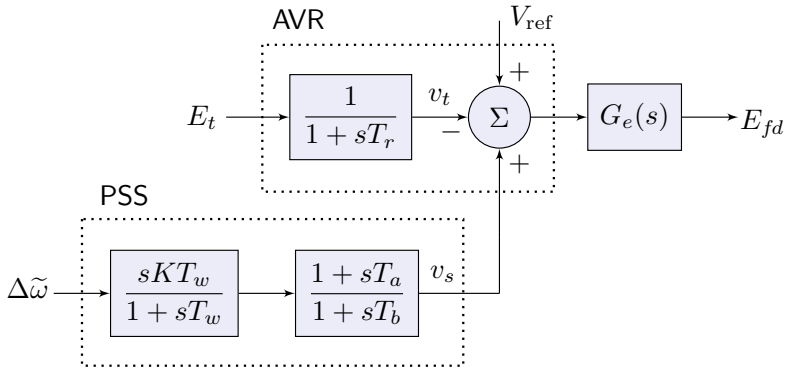

Figure 2.2: Excitation system with AVR and PSS, where $G_e(s)$ represents the transfer function of the exciter.

and β_2 are equal and nonzero the feedback signal becomes $\widetilde{\omega}(t) = \omega_i(t)$. Figure 2.2 shows how the simplified PSS block diagram fits in the context of an excitation system with an AVR. This form is equivalent to the one outlined in (2.13)–(2.15) provided that the downstream gain K is scaled appropriately.

2.2.5 Comparison With Existing PSS Models

This subsection compares the generalized $\Delta\omega$-type PSS with two industry-standard stabilizer designs: PSS2C and PSS4C. As described in the IEEE recommended practice for excitation system models [2], PSS2C represents a flexible dual-input stabilizer. This model supersedes and is backward compatible with PSS2A and PSS2B. It may be used to represent two distinct implementation types:

1) stabilizers that utilize two inputs to estimate the integral of accelerating power, and

2) stabilizers that utilize rotor speed (or frequency) feedback and incorporate a signal proportional to the electrical power as a means of compensation.

The generalized $\Delta\omega$-type PSS presented here bears similarities to the second of these types. The term in (2.11) multiplied by β_1 also represents a local rotor speed combined with an

auxiliary signal. The first key difference is that $\overline{\omega}(t)$ in (2.11) is synthesized from from wide-area, rather than strictly local, measurements. The second is that the generalized $\Delta\omega$ PSS also provides the ability to independently adjust the amount of steady-state error included in the feedback. In contrast, PSS2C does not feature a multi-band compensation mechanism.

For multi-band compensation, we turn to PSS4C which builds upon the structure originally proposed in [22]. As discussed in Section 2.1.1, the primary difference between the generalized $\Delta\omega$ PSS and PSS4C is the way the compensation is implemented. The PSS4C structure uses parallel lead-lag compensators to delineate the frequency bands, whereas the generalized $\Delta\omega$ PSS uses the linear combination of steady-state and small-signal components in (2.11). As shown in Section 2.4, the latter strategy provides of a means of achieving selective attenuation with minimal impact on the phase response. For an in-depth comparison of PSS2B and PSS4B, the precursors of the models discussed here, see [30].

2.3 Two-Area System Analysis

To study the impact of the control strategy outlined in Section 2.2, a combination of time- and frequency-domain analysis was employed. A custom dynamic model based on the block diagram shown in Figure 2.1 was implemented in the MATLAB-based Power System Toolbox (PST) [10]. This application facilitates not only time-domain simulation of nonlinear systems but also linearization and modal analysis. Two test systems were studied: a small model based on the Klein-Rogers-Kundur (KRK) two-area system [33], and a reduced-order model of the Western Interconnection. This section summarizes the results of analyzing the two-area test system. It comprises 13 buses, 14 branches, and 4 synchronous generators. A oneline diagram of the system is shown in Figure 2.3. In both models, the active component of the system load is modeled as constant current and the reactive component as constant impedance.

To permit study of transient disturbances, several modifications were made to the original KRK system. The synchronous machines in the standard case are representative of aggregate

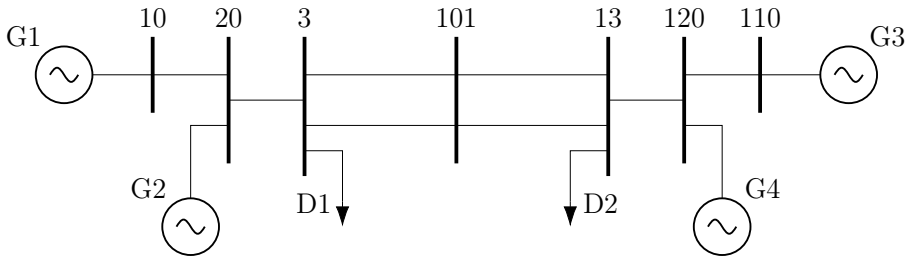

Figure 2.3: Oneline diagram of the two-area test system.

groups of generators concentrated in each area. Each unit has the same capacity and inertia. Hence, tripping any one generation unit offline would be equivalent to losing 25 % of the rotating inertia online in the system. To facilitate the study of realistically-sized generator trips, the capacity was redistributed such that each area possessed one machine representative of a collection of generators and the other a large individual plant. Generators G1 and G3 were scaled such that they each represented 5 % of the overall system capacity. The remainder was equally split between G2 and G4. Every unit in the system was then outfitted with the generalized $\Delta\omega$ PSS described in Section 2.2.

2.3.1 Sensitivity of System Poles to the PSS Tuning Parameters

Here we examine the effects of sweeping the PSS tuning parameters β_1 and β_2 on the poles of the system. The modal analysis was performed by linearizing the system dynamics and then solving for the eigenvalues and eigenvectors of the system matrix. The main result is that the oscillatory modes effectively split into two groups, one that is sensitive to changes in β_1 and the other β_2. Let us begin by examining the effect of the tuning parameters on the inter-area and local modes. Consider the inter-area mode indicated by the blue x located at 0.76 Hz in Figure 2.4. The shape of this mode observed through the machine speeds is shown in Fig. 2.5(a). Recall that mode shape is defined by the elements of the right eigenvector corresponding to the states of interest [54]. As demonstrated by Fig. 2.5(a), this mode is characterized by generators G1 and G2 oscillating against G3 and G4. The two-area system

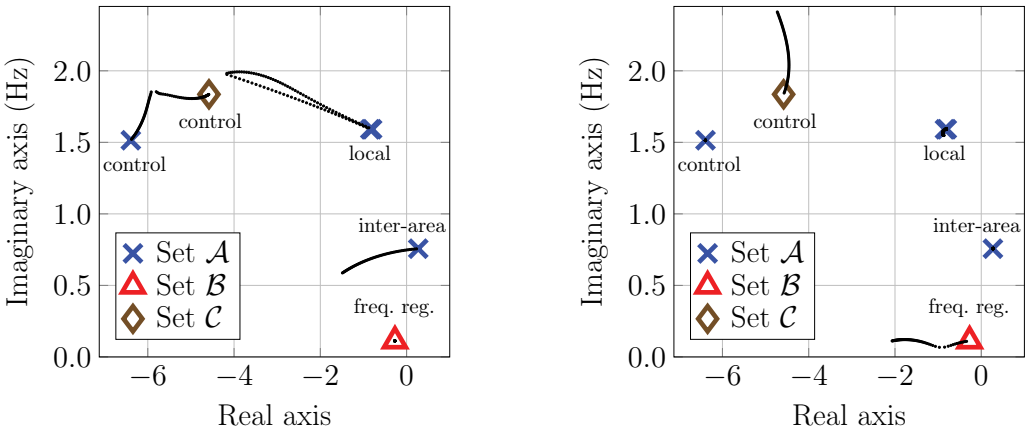

(a) β_1 parameter sweep. (b) β_2 parameter sweep.

Figure 2.4: Sensitivity of the system oscillatory modes to the PSS tuning parameters. The modes in $\mathcal{A}$ are sensitive to changes in β_1, those in $\mathcal{B}$ to β_2, and those in $\mathcal{C}$ to both.

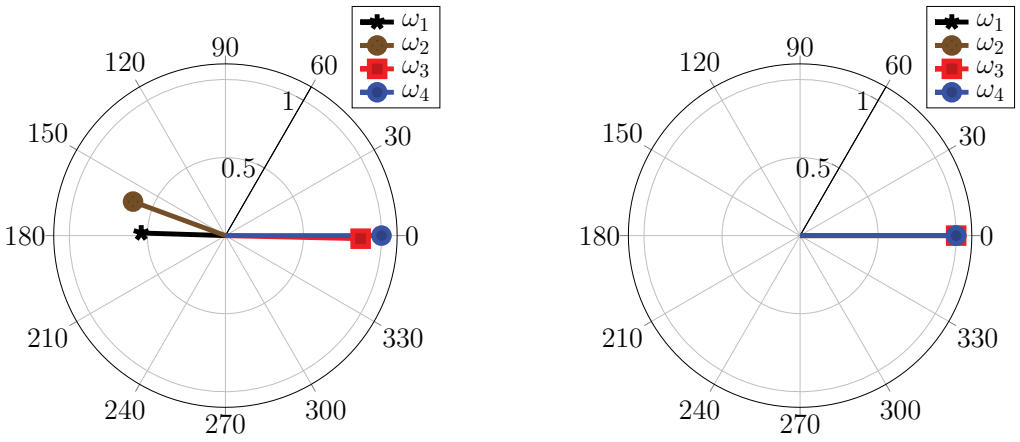

(a) 0.76 Hz inter-area mode. (b) 0.09 Hz freq. regulation mode.

Figure 2.5: Normalized mode shape plots for the two-area system.

is tuned such that this inter-area mode is unstable without supplemental damping control.

The plots in Figure 2.4 show the sensitivity of the system poles to the PSS tuning parameters. To generate these plots, either β_1 or β_2 was swept over an interval while the other was held at zero. The tuning parameters for all of the PSS units were swept in unison,

and the gain was uniformly held fixed at $K = 25$. Sweeping the tuning parameters for all units together facilitates study of the effect of PSSs on the frequency regulation mode. In Fig. 2.4(a), β_1 was swept over the interval $[0, 1]$ while β_2 was held at zero. As β_1 increases, the inter-area mode moves to the left and decreases slightly in frequency. The local modes, indicated by the blue x's in the upper right quadrant of Fig. 2.4(a), move to the left and increase slightly in frequency. A well-controlled exciter mode marked by the blue x in the upper left quadrant moves up and to the right but remains comfortably in the left half of the complex plane. For all intents and purposes, the frequency regulation mode is unaffected by changes in β_1. Hence, β_1 dictates the extent to which the PSS damps inter-area and local modes of oscillation.

The parameter β_2 primarily influences the frequency regulation mode. This mode is indicated by the red triangle located at 0.09 Hz in Figure 2.4. The shape of the frequency regulation mode observed through the machine speeds is shown in Fig. 2.5(b). All of the machine speeds are in phase and have nearly identical magnitudes. In Fig. 2.4(b), the parameter β_2 was swept over the interval $[0, 1]$ while β_1 was held at zero. As β_2 increases, the frequency regulation mode moves to the left. The higher-frequency exciter mode marked with a diamond moves upward. This control mode exhibits some sensitivity to both β_1 and β_2. In contrast, the inter-area and local modes are relatively unaffected by changes in β_2. The dependence of the frequency regulation mode on β_2 indicates that PSSs, in aggregate, play an important role in shaping the system response to transient disturbances. To demonstrate this phenomenon, and the effects of the PSS tuning parameters more broadly, we present a collection of time-domain simulations.

2.3.2 Time-Domain Simulations

The two-area system was simulated in PST for a variety of PSS tunings. As in the frequency-domain analysis, all PSS units were tuned alike and used the same gain. The contingency of interest in this set of simulations is a trip of generator G3. This event was selected because it initiates a transient disturbance that excites not only the inter-area and local modes but

also the frequency regulation mode. In the first set of simulations, β_1 was varied over the set $\{0.33, 0.67, 1\}$ while β_2 was held fixed at 0.33. In the second set of simulations, β_1 was held fixed at 0.33 while β_2 was varied over the set $\{0, 0.33, 0.67\}$. For all simulations, the overall PSS gain was set to $K = 18$. The case where $\beta_1 = \beta_2 = 0.33$ corresponds to a standard $\Delta\omega$ stabilizer with a gain of $K = 6$. This set of simulations assumes ideal communication in the construction of the time-varying reference $\overline{\omega}(t)$. Section 2.4.3 addresses the effect of nonideal communication network performance.

Figure 2.6 shows the key results for the case where β_1 is varied. The upper subplot shows the difference in speed between generators G2 and G4, *i.e.*, $\omega_2(t) - \omega_4(t)$. The oscillatory content in this signal is dominated by the 0.76 Hz inter-area mode. As β_1 increases, the damping of this mode also increases. The lower subplot shows the terminal voltage of generator G4. As β_1 is varied, the large-signal trajectory of the terminal voltage and its post-disturbance value are unchanged. This reflects the fact that varying β_1 only alters the small-signal characteristics of the field current.

Figure 2.7 shows the key results for the case where β_2 is varied. The upper subplot shows the system frequency response, which readily shows the behavior of the frequency regulation mode. The results show that β_2 plays a key role in determining the depth of the frequency nadir. The frequency nadir improves significantly as β_2 increases from 0 to 0.33, and modestly as it goes from 0.33 to 0.67. Effectively, β_2 determines the level of overshoot in the system step response. The lower subplot shows the terminal voltage of generator G4. As β_2 is increased, the terminal voltage following the generator trip becomes incrementally more depressed. This can be attributed to the fact that β_2 controls the extent to which steady-state changes in rotor speed are included in the PSS control error.

The process that causes β_2 to affect the frequency nadir is indirect. Increasing β_2 amplifies the steady-state component of the control error in (2.11). This depresses the field current supplied by the exciter and causes the voltage induced in the stator to dip. The electrical load decreases in response to this voltage dip with the amount of relief depending on the sensitivity of the load with respect to voltage. This tends to reduce the time-varying mismatch in

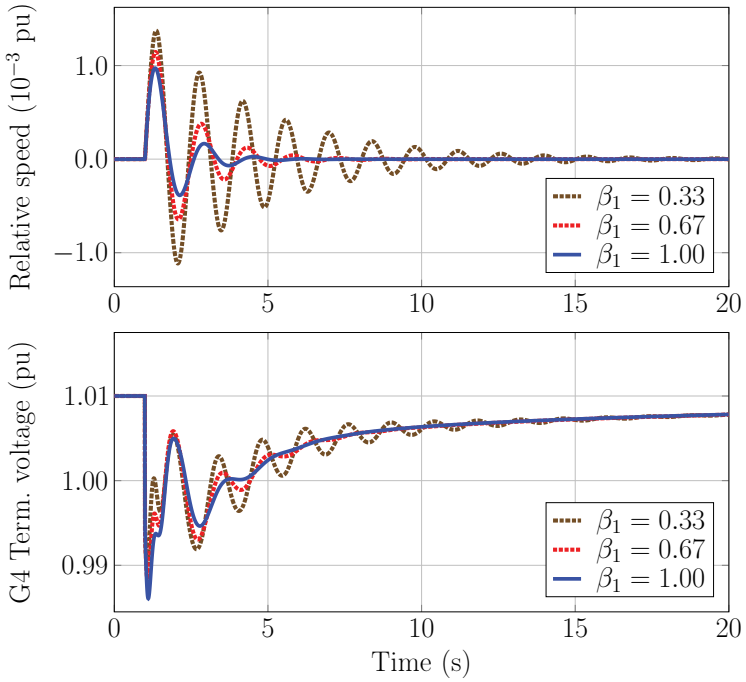

Figure 2.6: Time-domain simulations of generator G3 being tripped offline for various values of β_1. The top subplot shows the relative speed between G2 and G4.

mechanical and electrical torque, which improves the frequency nadir. This effect depends on the load composition, and the amount of improvement in the nadir decreases as the fraction of constant power load increases. Thus, there is a trade-off between improving the frequency nadir and degrading the voltage response. As explained in [15], the tendency of the PSS to counteract the voltage signal sent to the exciter by the AVR can reduce synchronizing torque and degrade transient stability. The control strategy presented in this chapter makes it possible to fine-tune the interaction between the PSS and AVR without affecting the damping of inter-area and local modes, and vice versa.

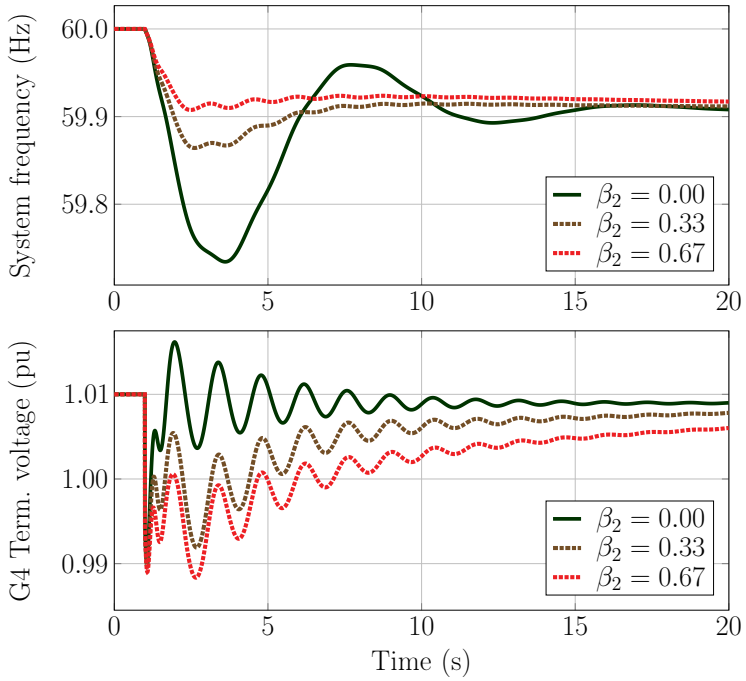

Figure 2.7: Time-domain simulations of generator G3 being tripped for various values of β_2.

2.4 Large-Scale Test System Analysis

For the two-area system discussed in Section 2.3, the inter-area and local modes were influenced by β_1, and the frequency regulation mode by β_2. This section addresses whether this property is preserved for large-scale systems. We consider a reduced-order model of the Western Interconnection named the *miniWECC*, in reference to the Western Electric Coordinating Council (WECC). It comprises 122 buses, 171 ac branches, 2 HVDC lines, and 34 synchronous generators. This system spans the entirety of the interconnection including British Columbia and Alberta. Its modal properties have been extensively validated against real system data [58, 59]. The aim of this analysis is to illustrate the fundamental behavior of various aspects of the proposed architecture in a controlled setting. Prior to implementation, high-fidelity simulation studies that account for variation in PSS structure and the dynamics of inverter-coupled generation would be required.

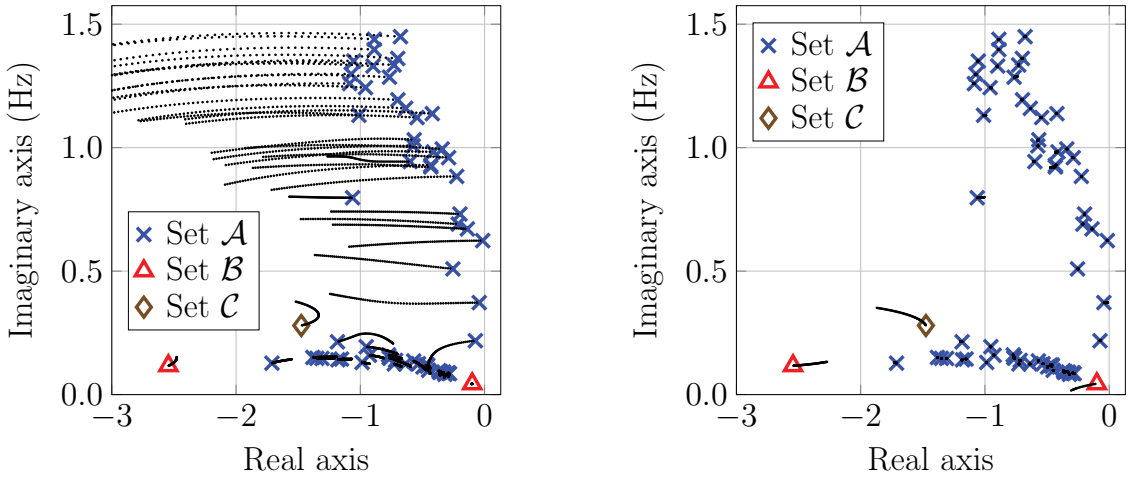

(a) β_1 parameter sweep.

(b) β_2 parameter sweep.

Figure 2.8: Sensitivity of the miniWECC oscillatory modes to the PSS tuning parameters. The modes in $\mathcal{A}$ are sensitive to changes in β_1, those in $\mathcal{B}$ to β_2, and those in $\mathcal{C}$ to both.

2.4.1 Sensitivity of System Poles to the PSS Tuning Parameters

To examine the sensitivity of the oscillatory modes to the PSS tuning parameters, the method described in Section 2.3.1 was applied to the miniWECC. Every generation unit in the system was outfitted with a generalized $\Delta\omega$ PSS with the gain set to $K = 25$. In practice, WECC policy dictates that "a PSS shall be installed on every synchronous generator that is larger than 30 MVA, or is part of a complex that has an aggregate capacity larger than 75 MVA, and is equipped with a suitable excitation system" [66]. Figure 2.8 shows the movement of the system poles in response to changes in the tuning parameters. In each subplot, either β_1 or β_2 was swept over an interval while the other was held at zero. The main result matches the one observed for the two-area system. The inter-area and local modes are influenced by β_1, and the frequency regulation mode by β_2. For the miniWECC, there is one well-controlled exciter mode marked with a diamond (near 0.28 Hz) that exhibits sensitivity to both parameters.

2.4.2 Open-Loop Frequency Response Analysis

The frequency-domain analysis presented in Sections 2.3 and 2.4.1 focused on a system-wide perspective. Here we provide a unit-specific analysis of the open-loop frequency response for a single generator. Outfitting a single unit with a PSS yields the state-space representation

$$\dot{x}(t) = Ax(t) + B_p u(t) \tag{2.18}$$

$$y_\nu(t) = C_\nu x(t), \tag{2.19}$$

where B_p describes how the system states are affected by changes in the PSS control input. The closed-loop control action determined by (2.13) can be implemented with the input

$$u(t) = -Ky_\nu(t) = -KC_\nu x(t) \tag{2.20}$$

$$u(t) = -K\begin{bmatrix} 0 & \gamma_1 & \gamma_2 & \dots & -\beta_1 \end{bmatrix}\begin{bmatrix} \widehat{x}(t) \\ f_1(t) \\ f_2(t) \\ \vdots \\ \omega_i(t) \end{bmatrix}, \tag{2.21}$$

where K is a scalar gain. The output matrix C_ν combines the states to form the PSS feedback signal $\nu(t)$. Note the presence of the extra negative sign to conform to the negative feedback convention. The state vector x in (2.21) is organized with the unused states $\widehat{x}$ on top, followed by the frequency measurements and the local rotor speed. For the kth sensor $\gamma_k = \alpha_k(\beta_1 - \beta_2)/f_0$, where α_k stems from the linear combination in (2.10), and f_0 is the nominal system frequency. In this analysis, the frequencies were computed by applying a derivative-filter cascade to the bus voltage angles as described in [51]. Hence, the unity-gain open-loop transfer function between a change in the PSS reference ν_{ref} and the feedback signal ν is

$$H(s) = C_\nu(sI - A)^{-1}B_p. \tag{2.22}$$

Figure 2.9 shows a high-level block diagram of the feedback loop for a single generation unit outfitted with a generalized $\Delta\omega$ PSS. Here $G_c(s)$ represents the PSS, $G_p(s)$ the plant,

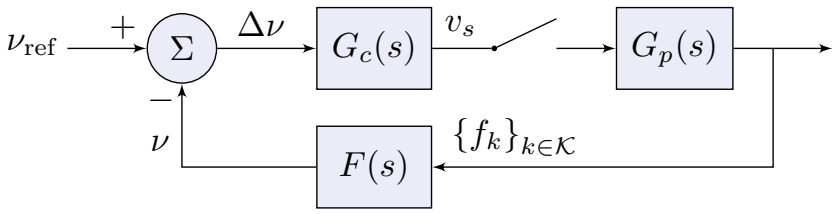

Figure 2.9: Feedback loop for a single generation unit outfitted with a generalized $\Delta\omega$ PSS, where $G_c(s)$ represents the controller, $G_p(s)$ the plant, and $F(s)$ the feedback process.

and $F(s)$ the feedback process. The exciter dynamics are included in $G_p(s)$, and the input to the plant represents a change in the exciter voltage reference V_{ref}. By commutativity, it holds that

$$H(s) = G_c(s)G_p(s)F(s) = G_p(s)F(s)G_c(s). \tag{2.23}$$

Hence, the loop transfer function between $\Delta\nu$ and ν is the same as the transfer function between a change in the exciter voltage reference V_{ref} and the output of the PSS v_s. Using this function, we can evaluate the effect of the PSS tuning parameters on the open-loop frequency response. For this analysis, only the unit being studied was outfitted with a PSS.

Figure 2.10 shows the effect of β_1 on the open-loop frequency response for generator G2, a hydroelectric unit in eastern British Columbia, where $\beta_2 = 1$ for all traces. The peak in the amplitude response near 0.04 Hz corresponds to the frequency regulation mode. As the plot shows, β_1 has no effect on the gain of the system at this frequency. This corroborates the system-wide modal analysis done in Sections 2.3 and 2.4.1 at the unit level. As expected, β_1 does change the amplitude response for the inter-area and local modes of oscillation. Unlike traditional compensation methods, this approach does not degrade the phase response in the attenuation region. As β_1 is varied, the phase response at the frequencies of the dominant amplitude peaks (0.37 Hz, 0.62 Hz, and 1.0 Hz) is essentially unchanged. The observed transition in phase through 0° at the resonant frequencies is ideal for damping control.

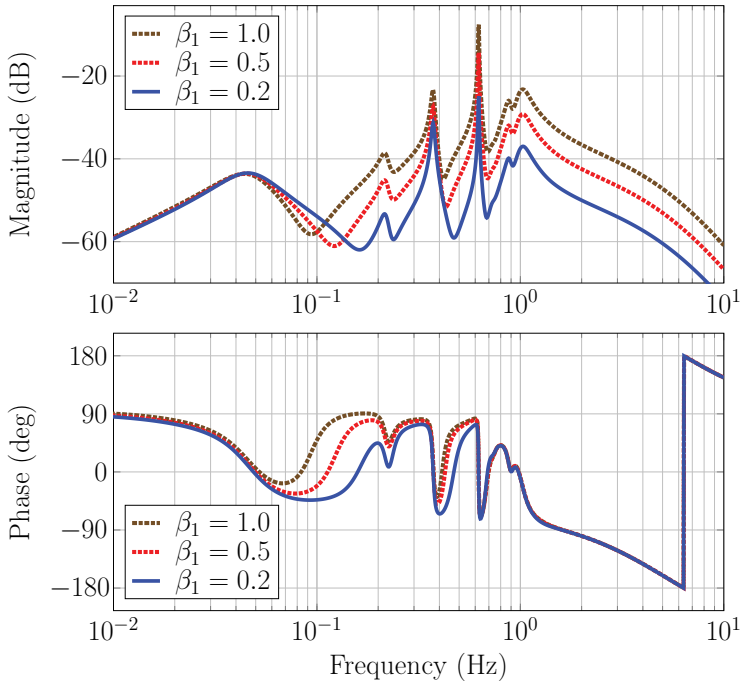

Figure 2.10: The effect of β_1 on the open-loop frequency response between the input to the exciter and the output of the generalized PSS for generator G2.

Figure 2.11 shows the effect of β_1 on the overall PSS compensation. As in [28], the uncompensated open-loop frequency response, including the washout filter dynamics, is provided for comparison. The overall compensation comprises both the lead-lag compensator and the tuning determined by β_1, β_2. When $\beta_1 = \beta_2 = 1$, the tuning stage has a gain of unity and imparts no phase shift. Hence, all of the compensation stems from the lead-lag compensator. This is expected because the case where $\beta_1 = \beta_2 = 1$ yields a standard $\Delta\omega$ stabilizer as shown in Table 2.1.

Figure 2.12 shows the effect of β_2 on the open-loop frequency response where $\beta_1 = 1$ for all traces. As β_2 is varied, the amplitude response at the frequencies corresponding to the local and inter-area modes is effectively unchanged. In contrast, the gain at the frequency regulation mode is reduced by roughly 14 dB as β_2 goes from 1 to 0.2. For $\beta_2 = 0.2$, the phase response

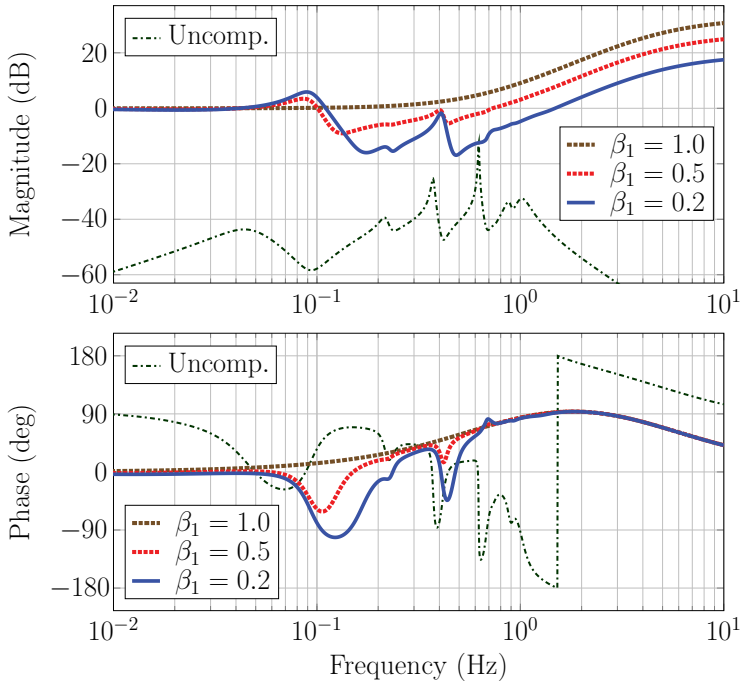

Figure 2.11: The effect of β_1 on the overall PSS compensation for generator G2 with the washout filter included in the uncompensated frequency response.

at the frequency regulation mode leads the case where $\beta_2 = 1$ by roughly 35°. This suggests that if a β_2 value below some nominal threshold is required for a particular application, it may be necessary to retune the lead-lag compensator and/or washout filter to ensure satisfactory low-frequency performance. The effect of β_2 on the overall PSS compensation is shown in Figure 2.13.

2.4.3 Co-Simulation of Power and Communication Systems

All of the analysis presented in Sections 2.3 through 2.4.2 was performed under the assumption of ideal communication. In this section, we analyze the effect of communication delay in the frequency domain and verify the findings in the time domain, as in [68]. The mathematical modeling developed here represents the real-time exchange of synchronized

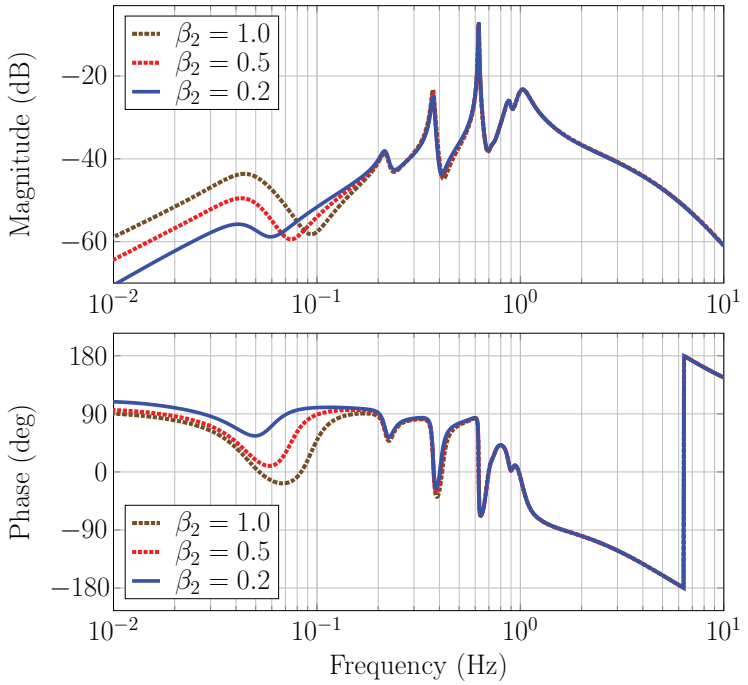

Figure 2.12: The effect of β_2 on the open-loop frequency response between the input to the exciter and the output of the generalized PSS for generator G2.

phasor measurement data over a network. As described in the IEEE standard governing data transfer in PMU networks [1], communication delays in WAMS are typically in the range of 20–50 ms; however, the combined delay must also account for the effect of transducers, processing, concentrators, and multiplexing [47, 69, 77]. In [47], the delay attributed to these factors is estimated at 75 ms, which yields an approximate range of 95–125 ms for the combined delay. This range is reflective of systems that utilize fiber-optic communication. It aligns closely with the experimental results reported in [51], 69–113 ms, but may vary depending on the communication method employed, *e.g.*, wired vs. wireless. Here we evaluate scenarios with delays that are 5 to 10 times greater than the high end of this range.

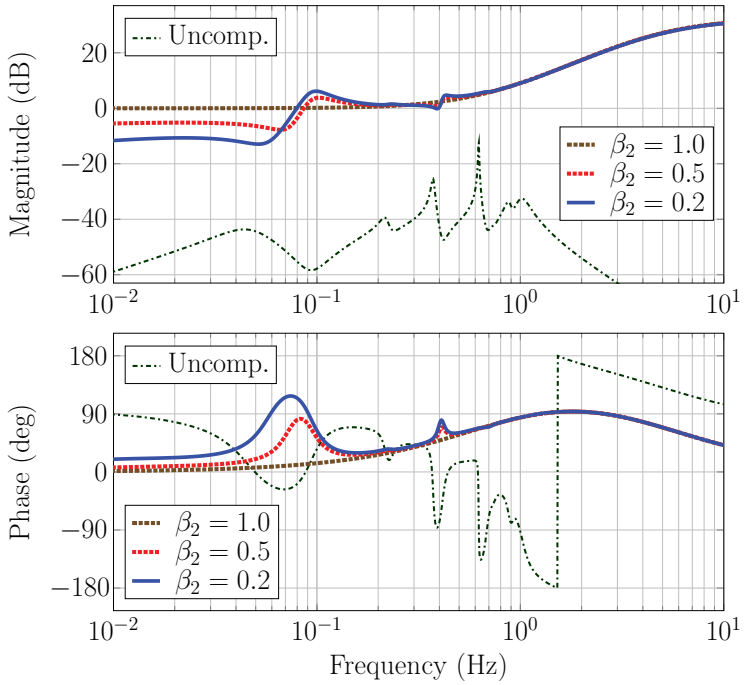

Figure 2.13: The effect of β_2 on the overall PSS compensation for generator G2 with the washout filter included in the uncompensated frequency response.

Modifying the state-space output matrix in (2.21) to account for delays as in [70], we have

$$\widehat{C}_\nu(s) = \begin{bmatrix} 0 & \gamma_1 e^{-s\tau_1} & \gamma_2 e^{-s\tau_2} & \dots & -\beta_1 \end{bmatrix} \tag{2.24}$$

$$\widehat{H}(s) = \widehat{C}_\nu(s)[sI - A]^{-1} B_p, \tag{2.25}$$

where τ_k is the delay of the kth sensor. Thus, the output matrix changes as a function of frequency. The open-loop transfer function with delay is given by (2.25). Figure 2.14 shows the results of using (2.25) to evaluate the effect of delay on the open-loop frequency response for generator G2 with $\beta_1 = 1$ and $\beta_2 = 0.5$. For simplicity, $\tau_k = \tau$ for all k. The entries of (2.24) correspond to the case where the local signal is not delayed, and the local and remote measurements are not time-aligned upon arrival. As a result, $\widehat{H}(s) \neq H(s)e^{-s\tau}$. In the extreme case where $\tau = 1.25\,\text{s}$ shown in Figure 2.14, the gain and phase are altered slightly in the neighborhood of the frequency regulation mode; however, the control performance and

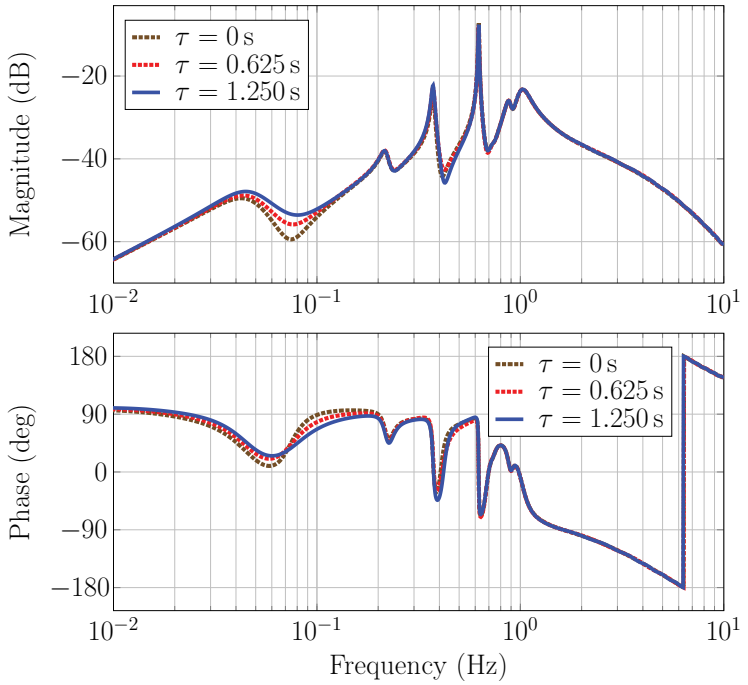

Figure 2.14: The effect of the combined delay τ on the open-loop frequency response for generator G2 with $\beta_1 = 1$ and $\beta_2 = 0.5$.

stability margins are essentially unchanged.

To study the impact of nonideal communication performance in the time domain, we used a co-simulation framework called HELICS [49]. A communication network model for the miniWECC was developed in ns-3 [53]. It features PMU endpoints that communicate with the controllers via the User Datagram Protocol (UDP). This model includes transmission delay, congesting traffic, and packet-based error emulation. Each generation unit in the PST model was outfitted with a generalized $\Delta\omega$ PSS where $\beta_1 = 1$, $\beta_2 = 0.5$, and $K = 9$. Figure 2.15 shows time-domain simulations of generator G26, a large nuclear plant in Arizona, being tripped offline for various expected delays $\overline{\tau}$. The results are in close agreement with the frequency-domain analysis shown in Figure 2.14. Thus, for this example, the benefits of the control strategy are retained even under pessimistic assumptions of communication

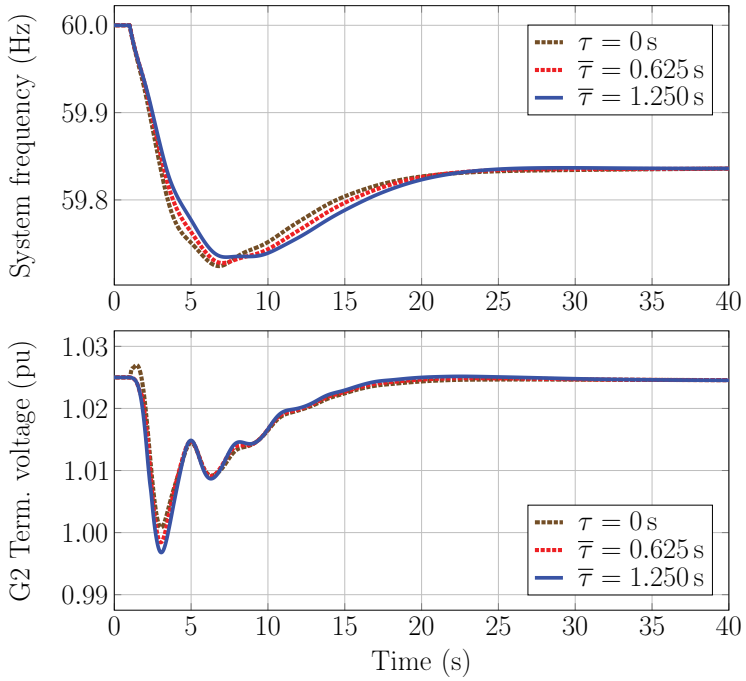

Figure 2.15: Simulations of generator G26 being tripped offline for various average combined delays where $\beta_1 = 1$ and $\beta_2 = 0.5$.

network performance.

In the miniWECC examples discussed herein, the center-of-inertia speed estimate $\overline{\omega}(t)$ was synthesized using 30 sensors geographically distributed throughout the system. The effect of delay on the open-loop frequency response is dependent on the number and placement of the frequency (or speed) sensors. These factors determine how well $\overline{\omega}(t)$ tracks the target defined in (2.9). By extension, they also influence its spectral content. When $\overline{\omega}(t)$ approximately tracks the true center-of-inertia speed, its amplitude spectrum is dominated by very low-frequency content, generally $\leq 0.1\,\mathrm{Hz}$. If too few sensors are used to synthesize this estimate, and/or those sensors are not adequately distributed, the amplitude spectrum of $\overline{\omega}(t)$ may include significant higher-frequency content, in and above the range of the electromechanical modes. If this occurs, the delay may impart larger deviations in the phase response above the

Table 2.2: Effect of Control Parameters on $\widehat{\gamma}_k$ Coefficients

Parameter Ratio	Coefficient Range
$\beta_2/\beta_1 < 1$	$0 < \widehat{\gamma}_k \leq \alpha_k/f_0$
$\beta_2/\beta_1 = 1$	$0 \leq \widehat{\gamma}_k \leq 0$
$\beta_2/\beta_1 > 1$	$-\infty \leq \widehat{\gamma}_k < 0$

frequency regulation mode than shown in Figure 2.14. For similar reasons, the coefficients of the linear combination in (2.10) also affect the relationship between the combined delay and the frequency response.

The other main factor influencing this relationship is the tuning determined by β_1, β_2. Analysis indicates that tunings where $\beta_1 < \beta_2$ may be more susceptible to the effects of delay than those where $\beta_1 \geq \beta_2$. To explore this behavior, we will analyze the entries of the output matrix $\widehat{C}_\nu(s)$. Let $\widehat{\gamma}_k = \gamma_k/\beta_1$. The matrix $\widehat{C}_\nu(s)$ may then be expressed as

$$\widehat{C}_\nu(s) = \beta_1 \Big[0 \quad \widehat{\gamma}_1 e^{-s\tau_1} \quad \widehat{\gamma}_2 e^{-s\tau_2} \quad \dots \quad -1 \Big], \tag{2.26}$$

where

$$\widehat{\gamma}_k = \frac{\alpha_k}{f_0}\left(1 - \frac{\beta_2}{\beta_1}\right). \tag{2.27}$$

Recall from (2.10) that the weights α_k are nonnegative and sum to one. For all real $\omega\tau$, it holds that $|e^{-j\omega\tau}| = 1$. Thus, the relationship between the magnitudes of the entries of $\widehat{C}_\nu(s)$ corresponding to the delayed and non-delayed system states is primarily determined by the ratio β_2/β_1. Table 2.2 shows a breakdown of the possible cases. The term inside the brackets of (2.26) corresponding to the local rotor speed always has a magnitude of one. The magnitudes of the remaining entries may either be zero, bounded, or unbounded.

When $\beta_2/\beta_1 = 1$ the controller is immune to delay because $\widehat{\gamma}_k = 0$ for all k. This aligns with expectations because the case where $\beta_1 = \beta_2 \neq 0$ corresponds to a standard $\Delta\omega$ stabilizer, as shown in Table 2.1. When $\beta_2/\beta_1 < 1$, the magnitude of $\widehat{\gamma}_k$ has an upper bound of α_k/f_0.

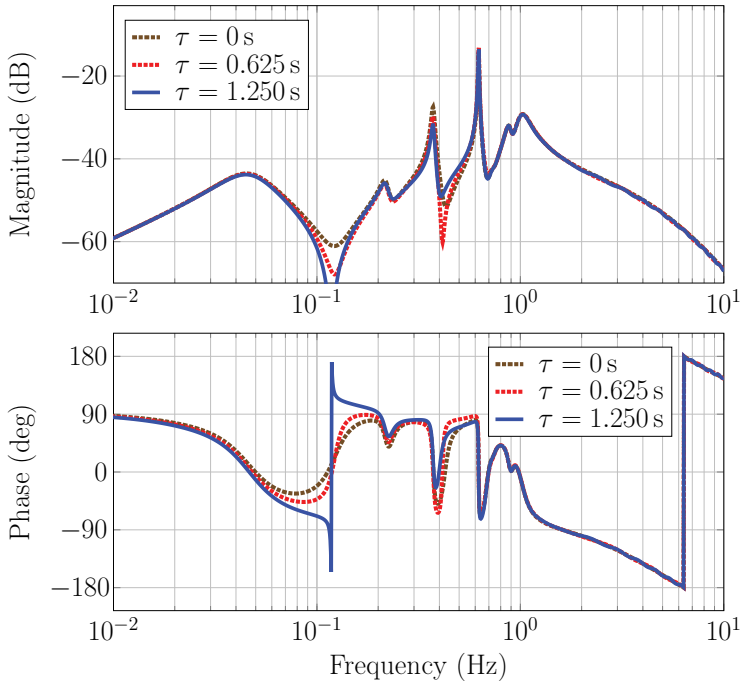

Figure 2.16: The effect of the combined delay τ on the open-loop frequency response for generator G2 with $\beta_1 = 0.5$ and $\beta_2 = 1$.

This corresponds to the case where $\beta_1 > \beta_2$, and the PSS prioritizes the damping of local and inter-area modes. When $\beta_2/\beta_1 > 1$, $\widehat{\gamma}_k$ is unbounded below. Thus, the magnitude of $\widehat{\gamma}_k$ may grow arbitrarily large as $\beta_1 \to 0$. This does not imply that $\widehat{C}_\nu(s)$ may have infinite values; rather, that the steady-state component of the control error (2.11) may be much larger than the small-signal component. This corresponds to the case where $\beta_1 < \beta_2$, and the PSS prioritizes shaping the system response to transient disturbances. It is observed that the sensitivity of the open-loop frequency response to delay increases as the ratio β_2/β_1 increases. We hypothesize that the driving factor in this relationship is that as β_2/β_1 grows, so too do the magnitudes of the entries of $\widehat{C}_\nu(s)$ corresponding to the delayed system states in relation to the non-delayed state(s). That is, when $\beta_1 \ll \beta_2$, it follows that $|\widehat{\gamma}_k| > 1$ for some k. This suggests that if $\beta_1 < \beta_2$, the ratio β_2/β_1 should be kept small.

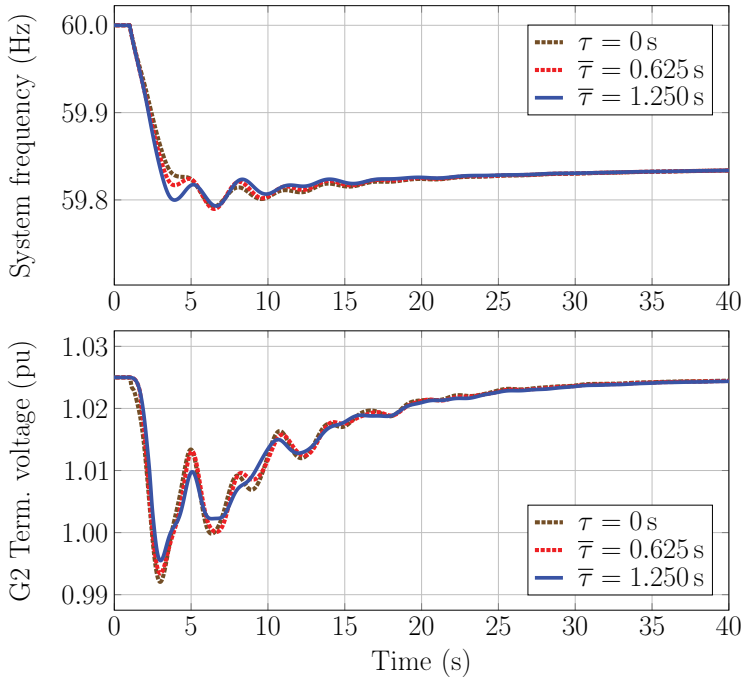

Figure 2.17: Simulations of generator G26 being tripped offline for various average combined delays where $\beta_1 = 0.5$ and $\beta_2 = 1$.

To illustrate this behavior, suppose that $\beta_1 = 0.5$, $\beta_2 = 1$ for generator G2, where $\beta_2/\beta_1 = 2$. Figure 2.16 shows the effect of delay on the open-loop frequency response for G2 in this case. As the delay increases, a key transfer function zero changes position in the complex plane. Figure 2.16 indicates that this zero is pushed across the $j\omega$-axis between 0.1–0.2 Hz and into the right half of the complex plane as the delay increases. Right-half-plane zeros, especially in the neighborhood of the electromechanical modes, may erode stability margins and are generally undesirable [11]. In this case, the system remains stable when $\tau = 1.25\,\mathrm{s}$ because the gain at the critical frequencies is very low.

Figure 2.17 shows the system response in the time domain following a trip of G26. Each generation unit in the PST model was outfitted with a generalized $\Delta\omega$ PSS where $\beta_1 = 0.5$, $\beta_2 = 1$, and $K = 9$. As the state trajectories show, this tuning places more emphasis on

shaping the transient response than on damping local and inter-area modes. Such parameter combinations should be used with caution. Careful stability analysis must be carried out to ensure that it is safe to employ a particular tuning given the performance characteristics of the measurement, communication, and control equipment.

2.5 Summary

This chapter presented a generalization of the standard $\Delta\omega$-type stabilizer. It works by incorporating local information with a real-time estimate of the center-of-inertia speed. The ability of the stabilizer to improve the damping of electromechanical modes is decoupled from its role in shaping the system response to transient disturbances. Hence, the interaction between the PSS and AVR can be fine-tuned based on voltage requirements. Future work will explore a variation of the proposed architecture that permits integral of accelerating power feedback for mitigating torsional oscillations. Finally, another interesting avenue of research will be developing online methods to optimally estimate the center-of-inertia frequency in the presence of delays, jitter, and measurement noise.

Chapter 3

A TRAJECTORY TRACKING WIDE-AREA CONTROLLER FOR STABILIZING TRANSIENT DISTURBANCES

This chapter presents a trajectory tracking control strategy that modulates the active power injected by geographically distributed inverter-based resources. Each resource is independently controlled, and its response drives the local bus voltage angle toward a trajectory that tracks the angle of the center of inertia. The center-of-inertia angle is estimated in real time from wide-area measurements. The main objectives are to stabilize transient disturbances and increase the amount of power that can be safely transferred over key transmission paths without loss of synchronism. Examples of suitable actuators include energy storage systems and partially-curtailed photovoltaic generation. The strategy stems from a time-varying linearization of the equations of motion for a synchronous machine. The control action produces synchronizing torque in a special reference frame that accounts for the motion of the center of inertia. This drives the system states toward the desired trajectory and promotes rotor angle stability. For testing we employ a reduced-order dynamic model of the North American Western Interconnection. The results show that this approach improves system reliability and can increase capacity utilization on stability-limited transmission corridors.

3.1 Motivation

When power systems that lack sufficient synchronizing torque are subjected to a severe disturbance they may fail to maintain rotor angle stability [35]. To mitigate this risk, stability limits are imposed on certain transmission corridors that inhibit the full utilization of existing thermal capacity. In turn, this increases the investment and operation costs of the transmission system. With the exception of voltage regulation, engineers have generally turned to protection and remedial action schemes to respond to transient disturbances rather than feedback control systems [5]. The challenges of implementing the latter are twofold. First, stabilizing transient disturbances requires actuators that can rapidly respond to events such as faults, line outages, and generator trips. Second, as the system is pushed further away from its original stable equilibrium, constructing a suitable feedback signal solely from local information becomes increasingly difficult [75]. The combination of wide-area measurement systems (WAMS) and fast-acting inverter-based resources (IBRs) enables new approaches to address these problems.

Building upon the framework in Chapter 2, we develop a trajectory tracking control strategy for stabilizing transient disturbances. It modulates the active power injected by independently controlled, geographically distributed IBRs. Here we envision the actuators as utility-scale energy storage systems (ESS). The response of each actuator drives its local bus voltage angle toward a trajectory that tracks an estimate of the center-of-inertia angle synthesized from WAMS data. The overall strategy arises from a time-varying linearization of the equations of motion for a synchronous machine. The control response produces synchronizing torque in a special reference frame that accounts for the motion of the center of inertia. This drives the system states toward the desired nonequilibrium trajectory and promotes rotor angle stability. We employ a reduced-order dynamic model of the North American Western Interconnection called the *miniWECC* for testing [59]. The results show that this control strategy improves system reliability and can increase capacity utilization on stability-limited transmission corridors.

3.1.1 Literature Review

From a systems theory perspective, transient stability pertains to stability in the sense of Lyapunov [35]. Hence, it cannot be completely determined using linear analysis. One of the oldest and most important techniques for assessing transient stability is the *equal area criterion*. This graphical method provides valuable intuition about transient disturbances; however, its scope is limited to two-machine systems and the classical single-machine infinite bus framework. To address these limitations, alternative methods were sought that could be applied to more complex networks of synchronous machines. In [72], Xue *et al.* developed what they called the *extended* equal area criterion, which relied upon producing a two-machine equivalent model of the system. In parallel, there was a movement toward *direct methods* of determining transient stability, which do not require the solution of the differential equations, *i.e.*, simulated trajectories [27, 63]. Inspired by the efforts of Magnusson in [42], energy-based methods for stability analysis were developed and refined in [6, 7, 25, 48, 64].

Athay *et al.* put forth a seminal application of energy function analysis in [6]. They developed a system-wide energy function that accounted for the total change in rotor kinetic energy and potential energy. While useful, system-wide energy functions did not always provide insight into the mechanism of instability, or which critical machines, if any, were susceptible to loss of synchronism. Motivated by these factors, Vittal developed energy functions for individual machines using the concept of partial stability in [64]. The theory of partial energy functions was further extended in [45]. Limitations related to model accuracy and computational reliability impeded the adoption of direct methods in practice [35], but many core ideas were revisited in the context of *hybrid methods*. The defining characteristic of hybrid methods is that they combine energy function analysis with traditional time-domain simulation [43, 44, 56]. This approach sidesteps some of the challenges associated with direct methods while streamlining the process of determining stability margins. In Section 3.4, we use a hybrid approach inspired by [56] to study the impact of the proposed control strategy on system faults.

Numerous protection and remedial action schemes (RAS) have been developed to bolster transient stability [3, 8, 73, 78]. Also called *system protection schemes*, RAS initiate a predetermined action, or sequence thereof, in response to a particular condition or event [5]. In contrast, feedback control systems modulate the output of one or more actuators in response to an error signal. A majority of the control systems developed for transient stability regulate bus voltages using synchronous machine excitation systems and/or FACTS devices [23,38,65]. Related applications for series devices have also been explored [19,20,24]. Driven by economic and environmental factors, many contemporary large-scale power systems are experiencing rapid growth in the number of inverter-based resources. As the penetration of IBRs has grown, so too has interest in their potential to support transient stability [31,41,74]. In this work, we present a control strategy designed to stabilize transient disturbances by modulating the active power injected by IBRs. Examples of suitable actuators include energy storage systems and partially-curtailed photovoltaic generation.

3.1.2 Chapter Organization

The remainder of this chapter is organized as follows. Section 3.2 presents a time-varying linearization of the equations of motion for a synchronous machine. We then derive a trajectory tracking control strategy that emerges from this framework. In Section 3.3, we examine a set of large-scale sensitivity studies based on a reduced-order dynamic model of the Western Interconnection. Section 3.4 outlines the lessons learned from N-1 contingency analysis. It also covers a simplified path rating study for the California-Oregon Intertie. Section 3.5 summarizes and concludes.

3.2 Proposed Method

The accuracy of classical linearized models tends to decrease when the system operating point is driven away from the initial equilibrium. The findings of Chapter 2 indicate that linearizing the system dynamics around a trajectory can improve model performance under transient disturbances. A nonlinear representation of a system's dynamics is typically required to describe its response to transient disturbances. Given these developments, we base the wide-area control strategy on a time-varying linearization of the equations of motion for a synchronous machine. This section provides a primer on the definitions and theory of continuous-time linear time-varying (LTV) systems. We then show how the control strategy arises from these conceptual foundations.

3.2.1 Mathematical Preliminaries

Let $f : \mathbb{R}^n \times \mathbb{R}^m \to \mathbb{R}^n$ denote a nonlinear vector field

$$\dot{x}(t) = f(x(t), u(t)), \tag{3.1}$$

where $x(t) \in \mathbb{R}^n$ is the system state at time t and $u(t) \in \mathbb{R}^m$ the input. Linearizing f about a static equilibrium $\{x_0, u_0\}$ produces a linear time-invariant (LTI) system representation. Alternatively, linearizing about a nonequilibrium trajectory $\{\overline{x}(t), \overline{u}(t)\}$ produces a linear time-varying representation

$$\Delta\dot{x}(t) = A(t)\Delta x(t) + B(t)\Delta u(t), \tag{3.2}$$

where $\Delta x(t) = x(t) - \overline{x}(t)$ and $\Delta u(t) = u(t) - \overline{u}(t)$. In (3.2), the state-space matrices are functions of time

$$A(t) = D_x f(\overline{x}(t), \overline{u}(t)) \tag{3.3}$$

$$B(t) = D_u f(\overline{x}(t), \overline{u}(t)), \tag{3.4}$$

where the operator D_x returns the Jacobian matrix of partial derivatives with respect to x evaluated at time t, and D_u returns the analogous matrix of partials with respect to u.

3.2.2 Control Strategy Derivation

In this section, we derive a trajectory tracking control strategy by applying the concepts introduced in Section 3.2.1. Consider a synchronous machine connected to a large power system. In terms of per-unit accelerating power, the nonlinear equations of motion may be expressed as

$$\dot{\delta}(t) = \omega_b\Big[\omega(t) - \omega_0\Big] \tag{3.5}$$

$$\dot{\omega}(t) = -\frac{D}{2H}\Big[\omega(t) - \omega_0\Big] + \frac{1}{2H\omega(t)}\Big[P_m(t) - P_e(t)\Big], \tag{3.6}$$

where ω_0 is the per-unit synchronous speed, D the damping coefficient, and H the inertia constant. Recall that (3.5) describes the angular velocity of the rotor and (3.6) the acceleration. Now let $\mathfrak{D}(t)$ and $\mathfrak{T}(t)$ be time-varying coefficients defined as

$$\begin{bmatrix}\mathfrak{D}(t)\\ \mathfrak{T}(t)\end{bmatrix} \triangleq -2H\left[\begin{matrix}\dfrac{\partial\dot{\omega}}{\partial\omega}\\ \dfrac{\partial\dot{\omega}}{\partial\delta}\end{matrix}\right]\Bigg|_{\overline{x}(t),\overline{u}(t)}, \tag{3.7}$$

where the right-hand side represents the scaled partial derivatives of (3.6) taken with respect to the state variables ω and δ. These derivatives are evaluated about a state trajectory $\overline{x}(t)$ and input $\overline{u}(t)$. We show that when $\overline{x}(t)$ is selected appropriately, $\mathfrak{D}(t)$ is the damping coefficient in the center-of-inertia reference frame and $\mathfrak{T}(t)$ the synchronizing torque coefficient. For an in-depth analysis of the LTV damping coefficient $\mathfrak{D}(t)$, see Chapter 2.

The appropriate analytical form of $\mathfrak{T}(t)$ depends on the model being used to describe transmission network. In the special case of a single-machine infinite bus system, the electrical power output of the machine is given by

$$P_e(t) = \frac{EV}{X}\sin\delta(t), \tag{3.8}$$

where X is the sum of the synchronous reactance and the line reactance between the terminals of the machine and the infinite bus. The internal stator voltage magnitude is denoted by E

and the voltage magnitude at the infinite bus by V. Per convention, the infinite bus has a voltage angle of zero. Evaluating (3.7), the LTV synchronizing torque coefficient is

$$\mathfrak{T}(t) = \frac{EV}{X}\frac{\cos\overline{\delta}(t)}{\overline{\omega}(t)}, \tag{3.9}$$

where $\overline{\omega}(t)$ and $\overline{\delta}(t)$ specify the nonequilibrium state trajectory generically represented as $\overline{x}(t)$. The expression in (3.9) in could be readily modified to accommodate a third-order Heffron-Phillips model by allowing the internal stator voltage to vary with time. In the context of multi-machine models such as those described in [63], $\mathfrak{T}(t)$ follows from (3.7).

Linearizing (3.5) and (3.6) about a trajectory and expressing the result in terms of $\mathfrak{D}(t)$ and $\mathfrak{T}(t)$ yields

$$\Delta\dot{\delta}(t) = \omega_b\Delta\omega(t) \tag{3.10}$$

$$\Delta\dot{\omega}(t) = -\frac{\mathfrak{D}(t)}{2H}\Delta\omega(t) - \frac{\mathfrak{T}(t)}{2H}\Delta\delta(t) + \frac{1}{2H\overline{\omega}(t)}\Delta P_m(t). \tag{3.11}$$

The state deviations are given by $\Delta\delta(t) = \delta(t) - \overline{\delta}(t)$ and $\Delta\omega(t) = \omega(t) - \overline{\omega}(t)$, where $\overline{\delta}(t)$ denotes the nonequilibrium angle trajectory and $\overline{\omega}(t)$ the speed trajectory. Furthermore, $\Delta P_m(t) = P_m(t) - \overline{P}_m(t)$, where $\overline{P}_m(t)$ is the mechanical power input trajectory. As shown in Chapter 2, it is possible to increase damping and support small-signal stability by producing electrical torque that is in phase with the speed deviation between the rotor and the center of inertia. Here we develop a strategy for stabilizing transient disturbances that produces an electrical power injection that is in phase with $\Delta\delta(t)$.

3.2.3 Nonequilibrium Trajectory

The nonequilbrium trajectory about which the equations of motion are linearized is based on a real-time estimate of the angle of the center of inertia. The concept of the center of inertia was introduced in [57] to facilitate a decomposition of the system dynamics. This decomposition allowed for precise characterization of the system frequency and synchronous equilibria. Let h_i be the normalized inertia constant for the ith machine

$$h_i = \frac{H_i}{H_T} \quad H_T = \sum_{i\in\mathcal{I}} H_i, \tag{3.12}$$

where $\mathcal{I}$ is the set of all online synchronous machines. The center-of-inertia speed and angle are then defined such that

$$\widetilde{\omega}(t) = \sum_{i \in \mathcal{I}} h_i \omega_i(t) \tag{3.13}$$

$$\widetilde{\delta}(t) = \sum_{i \in \mathcal{I}} h_i \delta_i(t). \tag{3.14}$$

Let $\{\overline{\delta}_i(t), \overline{\omega}_i(t)\}$ be the nonequilibrium state trajectory. In the control strategy, $\overline{\delta}_i(t)$ represents the desired angle trajectory toward which unit i is driven.

The nonequilibrium speed trajectory corresponding to the center-of-inertia reference frame is

$$\overline{\omega}_i(t) = \widetilde{\omega}(t), \tag{3.15}$$

for all i in $\mathcal{I}$. Because the rotor speed and angle are dynamically linked, (3.15) has implications for the angle trajectory $\overline{\delta}_i(t)$. From (3.5), the center-of-inertia angle $\widetilde{\delta}(t)$ and the desired angle trajectory $\overline{\delta}_i(t)$ may be stated in terms of $\widetilde{\omega}(t)$ as

$$\widetilde{\delta}(t) = \widetilde{\delta}(t_0) + \omega_b \int_{t_0}^{t} \widetilde{\omega}(\tau) - \omega_0 \, d\tau \tag{3.16}$$

$$\overline{\delta}_i(t) = \overline{\delta}_i(t_0) + \omega_b \int_{t_0}^{t} \widetilde{\omega}(\tau) - \omega_0 \, d\tau. \tag{3.17}$$

The center-of-inertia speed appears in the integrand of both (3.16) and (3.17) because $\overline{\omega}_i(t) = \widetilde{\omega}(t)$.

Recall that the LTV angle deviation of the ith machine is defined as $\Delta\delta_i(t) = \delta_i(t) - \overline{\delta}_i(t)$. In order for the angle deviation to be zero in steady state, it must hold that

$$\overline{\delta}_i(t_0) = \delta_i(t_0), \tag{3.18}$$

where t_0 indicates a point in time where the system resides at a stable equilibrium. A consequence of (3.18) is that $\overline{\delta}_i(t)$ is, in general, different for each unit. Combining (3.16)–(3.18) to solve for the nonequilibrium angle trajectory yields

$$\overline{\delta}_i(t) = \widetilde{\delta}(t) - \widetilde{\delta}(t_0) + \delta_i(t_0). \tag{3.19}$$

Hence, $\overline{\delta}_i(t)$ is equal to the angle of the center of inertia plus a fixed offset $\delta_i(t_0) - \widetilde{\delta}(t_0)$. This offset represents the difference between the rotor angle of the ith unit and the angle of the center of inertia at the stable equilibrium observed at t_0. Thus, the nonequilibrium state trajectory $\{\overline{\delta}_i(t), \overline{\omega}_i(t)\}$ is fully described by (3.15) and (3.19).

3.2.4 Real-Time Trajectory Estimation

In a real-time control application, the center-of-inertia angle $\widetilde{\delta}(t)$ would need to be estimated using available measurements. The challenges posed by this problem fall mostly outside the scope of this work; however, we will discuss some core concepts here. At the time of this writing, rotor angle measurements are not generally available through wide-area measurement systems. Thus, it is not possible to directly calculate (3.14) onboard the controller. If a suitable estimate of the center-of-inertia speed is available, $\widetilde{\delta}(t)$ may be approximated as

$$\widetilde{\delta}(t) \approx c + \omega_b \int_{t_0}^{t} \widetilde{\omega}(\tau) - \omega_0 \, d\tau, \tag{3.20}$$

where c is a constant. In practice, (3.20) would be computed using numerical integration. Here we explore approximating (3.14) with a weighted average of bus voltage angle measurements

$$\widetilde{\delta}(t) \approx c + \sum_{k \in \mathcal{K}} \gamma_k \theta_k(t), \tag{3.21}$$

where $\theta_k(t)$ is the angle measurement signal reported by the kth sensor, γ_k the associated weight, and $\mathcal{K}$ the set of available sensors. The weights γ_k are nonnegative and sum to one, *i.e.*, $1^T\gamma = 1$. For simplicity, we consider the arithmetic mean $\gamma_k = 1/|\mathcal{K}|$ for all k, where $|\mathcal{K}|$ is the number of available sensors. The key outcomes of this work do not depend strongly on this choice.

In the trajectory tracking controller, the value of c is of little importance because the offset in (3.19) ensures that $\Delta\delta_i(t_0) = 0$. Thus, we may henceforth regard c as a free parameter or set it to zero. In (3.21), it may be convenient to set c such that

$$c = \sum_{k \in \mathcal{K}} -\gamma_k \theta_k(t_0) \implies \widetilde{\delta}(t_0) = 0. \tag{3.22}$$

Given nonideal sensors, the approach in (3.21) may be slightly more susceptible to measurement bias than (3.20); however, the dc offset of the reference signal is not critical in this application, as noted above. When estimating $\widetilde{\delta}(t)$ using angle measurements as in (3.21), care must be taken to ensure that phase wraps do not introduce discontinuities in the control error.

3.2.5 Control Structure Refinement

Many synchronous machine excitation systems possess the bandwidth necessary to produce a field current modulation that is in phase with $\Delta\delta_i(t)$; however, doing so may interfere with the coordination between the automatic voltage regulator and power system stabilizer. Hence, we will explore using inverter-based resources as the control actuators. In light of this, we restrict the feedback to bus voltage angle measurements rather than rotor angles. Let $\theta_j(t)$ be the local voltage angle measured at the jth actuator at time t. The wide-area angle reference $\widetilde{\theta}(t)$ is

$$\widetilde{\theta}(t) = \sum_{k \in \mathcal{K}} \gamma_k \theta_k(t), \tag{3.23}$$

where $\gamma_k = 1/|\mathcal{K}|$, which follows from (3.21). As in (3.19), we specify the desired angle trajectory for the jth actuator as

$$\overline{\theta}_j(t) = \widetilde{\theta}(t) - \widetilde{\theta}(t_0) + \theta_j(t_0). \tag{3.24}$$

In the examples given in this chapter, $\widetilde{\theta}(t)$ was synthesized from measurements reported by 36 simulated sensors distributed throughout the Western Interconnection. Each sensor was modeled as a first-order time constant with $T = 0.02\,\text{s}$. The effects of measurement noise and nonideal communication are considered in Section 3.4.

Given an appropriate choice of sign, (3.11) suggests that synchronizing torque can be produced by injecting real power that is in phase with $\Delta\theta_j(t) = \theta_j(t) - \overline{\theta}_j(t)$. By analyzing the LTI state deviations we can identify a control structure that is responsive not only to $\Delta\theta_j(t)$, but also to the movement of the center-of-inertia angle away from its pre-disturbance value. The LTI state deviations may be decomposed into two parts where one component

captures the difference between the state and a time-varying reference, and the other the difference between the reference and its pre-disturbance value.

Splitting the LTI control error $\theta_j(t) - \theta_j(t_0)$ into two parts and taking the linear combination yields

$$\Delta\xi(t) \triangleq \alpha_1\Big[\theta_j(t) - \overline{\theta}_j(t)\Big] + \alpha_2\Big[\overline{\theta}_j(t) - \theta_j(t_0)\Big], \tag{3.25}$$

where α_1 and α_2 are tuning parameters restricted to the unit interval. We examine the relative impact of these parameters in Section 3.3. The decomposition in (3.25) is performed by adding $\overline{\theta}_j(t) - \overline{\theta}_j(t) = 0$ to the LTI control error. Rearranging (3.24), we see that

$$\overline{\theta}_j(t) - \theta_j(t_0) = \widetilde{\theta}(t) - \widetilde{\theta}(t_0). \tag{3.26}$$

By substitution, the control error $\Delta\xi(t)$ in (3.25) may then be restated as

$$\Delta\xi(t) = \alpha_1\Big[\theta_j(t) - \overline{\theta}_j(t)\Big] + \alpha_2\Big[\widetilde{\theta}(t) - \widetilde{\theta}(t_0)\Big]. \tag{3.27}$$

This form makes it clear that the second term represents the deviation between the center-of-inertia angle and its pre-disturbance value. As a consequence, this component of the control error is theoretically the same for all controllers. In practice, there may be small differences arising from variation in the estimates of $\widetilde{\theta}(t)$.

The final structure of the wide-area synchronizing controller is shown in Figure 3.1. The upper sum at the input yields the component of the control error multiplied by α_1, and the lower sum the component multiplied by α_2. There are two separate compensation paths, each consisting of a washout (highpass) filter cascaded with a lead-lag compensator. The form of the filtering and phase compensation blocks is flexible, and multiple stages may be employed if necessary. Tuning considerations are discussed in Section 3.3. In the case of energy storage, p_s represents a change in the charging setpoint for positive values of K.

Figure 3.2 shows a converter interface where for simplicity it is assumed that the IBR injects only active power. The electrical controller shown in Figure 3.1 provides an auxiliary input to this interface. The structure in Figure 3.2 was based on the generic dynamic models for renewable energy systems developed in the Western Electric Coordinating Council

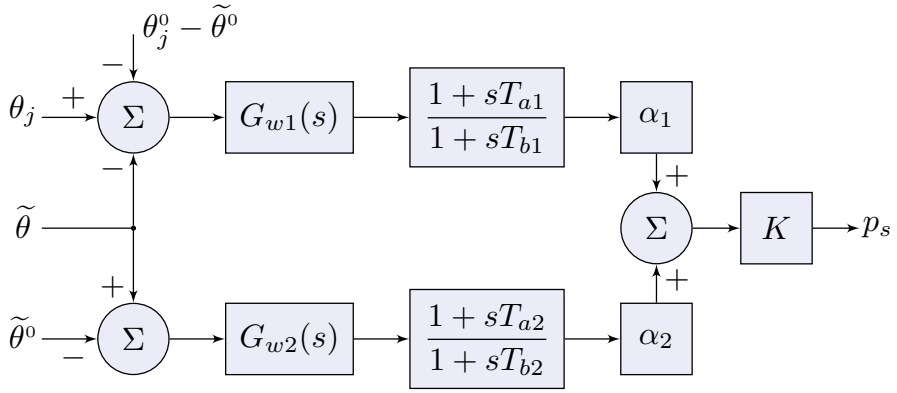

Figure 3.1: Block diagram of the trajectory tracking wide-area synchronizing controller. The $G_{w1}(s)$ and $G_{w2}(s)$ blocks represent washout (highpass) filters. The lead-lag compensation blocks are only used if necessary and may possess any number of stages.

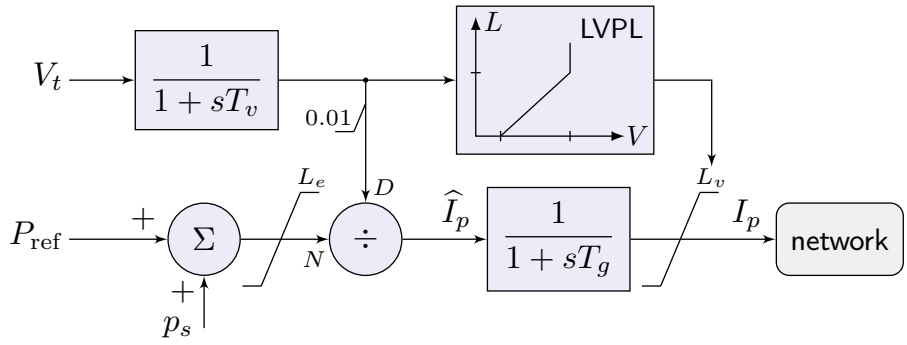

Figure 3.2: High-level diagram of the simplified converter interface. In the division operator N stands for numerator and D for denominator. The lower bound on the terminal voltage measurement prevents numerical errors and excessively large current commands. The *low-voltage power logic* (LVPL) block imposes voltage-dependent bounds on the injected current.

(WECC) [18]. In the saturation stage after the initial sum, the bounds on the commanded power account for device ratings and, if applicable, limits on the ESS state of charge. The commanded power is then divided by the terminal voltage magnitude to produce an active current command, $\widehat{I}_p$. In this step, a lower bound is placed on the voltage measurement

to prevent numerical errors and excessively large current commands. After accounting for the interface time constant, the current command is passed through a final saturation stage where the bounds are voltage dependent. This prevents the model from attempting to inject substantial active current into a faulted bus. For more information about this *low-voltage power logic* (LVPL), see [18]. In simulation, the output of the interface model specifies a boundary current injection for the network equations.

3.3 Large-Scale Sensitivity Studies

To further explore the control strategy introduced in Section 3.2, we present a collection of large-scale sensitivity studies. For simulation and dynamic analysis we employ the MATLAB-based Power System Toolbox (PST) [10]. A custom dynamic model based on the diagrams shown in Figs. 3.1 and 3.2 was implemented within the PST framework. The test case is based on a reduced-order dynamic model of the Western Interconnection, including British Columbia and Alberta, called the *miniWECC* [59]. It comprises 141 buses, 190 ac branches, 2 HVDC lines, and 34 synchronous generators. A total of 19 geographically distributed energy storage systems were installed in the miniWECC, one at each load center. Prior to implementation, high-fidelity simulation studies would be required to address issues such as non-unity power factor operation of the IBRs.

3.3.1 Time-Domain Analysis

This subsection examines the effect of sweeping the tuning parameters α_1 and α_2 on the time-domain system response. The aim is to build intuition about how the control strategy responds to disturbances, and how the resulting injections affect the state trajectories. Each of the 19 participating ESSs, rated at 100 MW/200 MWh, were configured identically for simplicity. These systems may correspond either to large individual ESSs or aggregated storage clusters. We consider a total ESS power capacity of 1.9 GW, which represents about 1.8 % of the overall miniWECC load. In all examples $G_{w1}(s)$ is a first-order highpass filter with a corner frequency at 0.1 Hz, and $G_{w2}(s)$ second-order with a corner near 0.01 Hz.

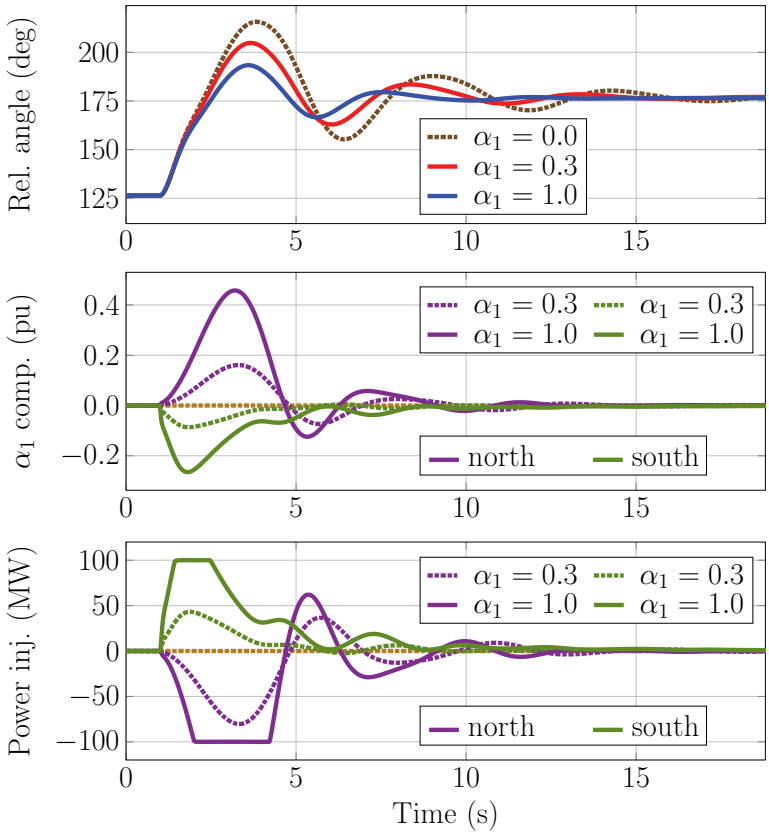

Figure 3.3: Time-domain simulations of generator G26 in Arizona being tripped offline for various values of α_1 where $\alpha_2 = 0$. The top subplot shows the relative angle between generator G34 in Alberta (north) and G23 in San Diego (south). The bottom two subplots show the behavior of the ESSs located near the load centers in Alberta and San Diego.

In the α_2 path, we included 15° of phase lead centered about the frequency regulation mode at 0.02 Hz. (For more information about the characteristics of the frequency regulation mode, see [17].) No phase compensation was required in the α_1 path. Lastly, the gain of each controller was held fixed at $K = 5$.

Figure 3.3 shows time-domain simulations of a large nuclear plant in Arizona being tripped offline for various values of α_1 where $\alpha_2 = 0$. This disturbance was selected because it excites all of the electromechanical modes of the system including the frequency regulation mode.

The top subplot shows the difference between the rotor angle of the representative generator in Alberta and the generator in San Diego. This pair represents the maximal inter-machine angle difference observed during the disturbance. The control effort has a stabilizing effect on this angle separation. In particular, we see that the frequency of the oscillatory component of the response rises, which indicates an increase in synchronizing torque.

The bottom two subplots show the behavior of the ESSs located near the load centers in Calgary (Alberta) and San Diego. The middle subplot shows the α_1 component of the control response, *i.e.*, the top input to the final summation block of Figure 3.1. Immediately following the disturbance, the speed of the machine in Alberta is slightly faster than the center-of-inertia speed, and the speed of the machine in San Diego slightly slower. This occurs because the machine in San Diego is closer (electrically) to the tripped generator than the average machine in the system, and the generator in Alberta farther away. Over the first swing of the transient, these relationships manifest themselves as a positive α_1 component in Alberta and a negative component in San Diego. Recall that this component of the response results from passing $\alpha_1[\theta_j(t) - \overline{\theta}_j(t)]$ through the controller compensation. To mitigate the system separation in the first swing, the ESS in Alberta charges and the one in San Diego discharges.

Figure 3.4 shows time-domain simulations of the same disturbance for various values of α_2 where $\alpha_1 = 0$. The top subplot shows the frequency of the center of inertia. The control effort has a stabilizing effect on the frequency response. As α_2 increases the depth of the nadir is reduced, and the frequency rebounds more quickly. The bottom two subplots show the behavior of a representative controller, which is the same for each ESS in this case. Recall that the α_2 component results from passing $\alpha_2[\widetilde{\theta}(t) - \widetilde{\theta}(t_0)]$ through the controller compensation. Neglecting the effects of nonideal communication, the center-of-inertia angle estimate $\widetilde{\theta}(t)$ is the same for all ESSs resulting in identical α_2 components. (We consider nonideal communication in Section 3.4.) When the speed of the center of inertia deflects downward, $\widetilde{\theta}(t)$ declines from its initial value value $\widetilde{\theta}(t_0)$. This results in a negative α_2 component that causes every ESS in the system to inject power that is in phase with the error.

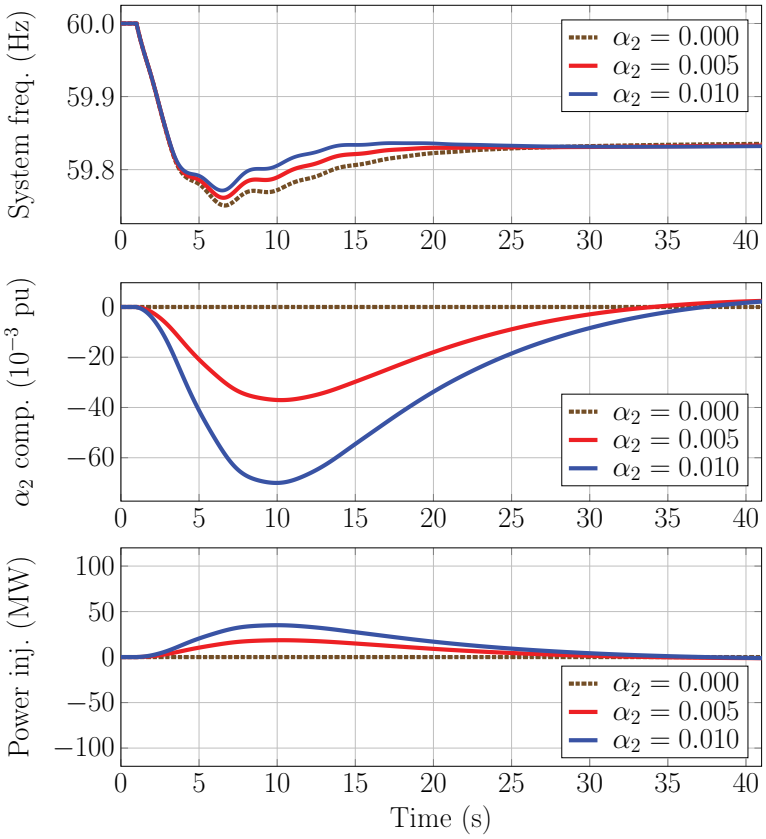

Figure 3.4: Time-domain simulations of generator G26 in Arizona being tripped offline for various values of α_2 where $\alpha_1 = 0$. The top subplot shows the frequency of the center of inertia. In this case all of the controllers synthesize identical estimates of $\widetilde{\theta}(t)$, so $\alpha_2[\widetilde{\theta}(t) - \widetilde{\theta}(t_0)]$ is the same for each ESS.

In a practical application, the total control response would effectively be a superposition of the injections depicted in Figs. 3.3 and 3.4.

3.3.2 Frequency-Domain Analysis

Linear analysis allows us to develop criteria that are *necessary but not sufficient* for ensuring acceptable transient stability control performance. For example, theory dictates that positive synchronizing torque drives the electromechanical modes of oscillation upward in the complex

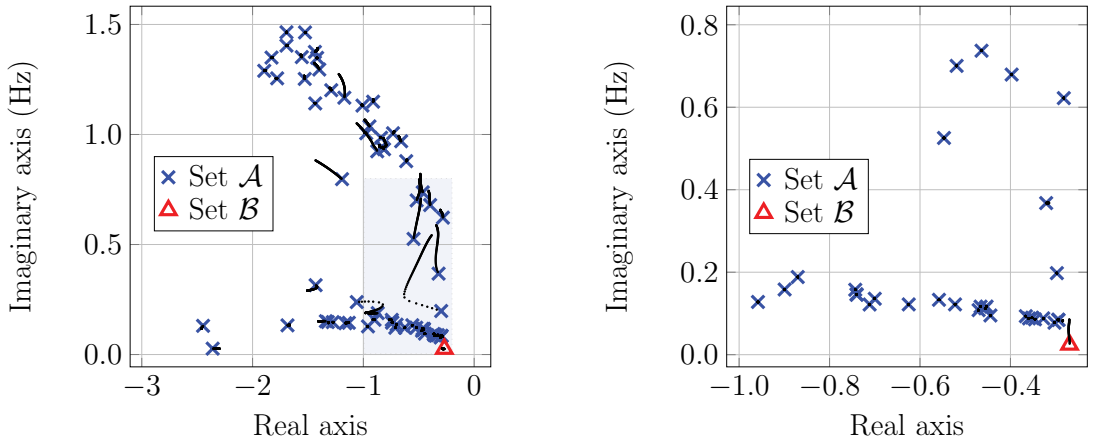

(a) α_1 parameter sweep.

(b) α_2 parameter sweep.

Figure 3.5: Sensitivity of the system oscillatory modes to the tuning parameters. The modes in $\mathcal{A}$ are sensitive to changes in α_1, and those in $\mathcal{B}$ to α_2. As shown, the only member of $\mathcal{B}$ is the frequency regulation mode. The shaded patch in (a) indicates the axis range of (b).

plane. Furthermore, the open-loop frequency response for each actuator must comply with the Nyquist stability criterion. Fig. 3.5(a) shows how the modes of the miniWECC respond when α_1 is swept over the interval $[0, 1]$ uniformly for all actuators, while $\alpha_2 = 0$ and $K = 30$. The electromechanical modes that are responsive to the control are either pushed directly upward, indicating pure synchronizing torque, or up and to the left, indicating a combination of damping and synchronizing. The frequency regulation mode, marked with a red triangle, is not sensitive to α_1. Conversely, Fig. 3.5(b) shows that as α_2 is swept over $[0, 0.1]$, the frequency regulation mode moves upward while the inter-area and local modes are unaffected. The phase lead introduced in the α_2 path ensures that the angle of departure of the frequency regulation mode is directly vertical, as opposed to slightly to the right.

Figure 3.6 shows the open-loop frequency response between a change in P_{ref} and the controller output p_s for the ESS located in British Columbia. In order to add synchronizing torque, the phase response would ideally transition through $-90°$ at each resonant frequency. We observe that the North-South A mode just above 0.20 Hz is not strongly observable

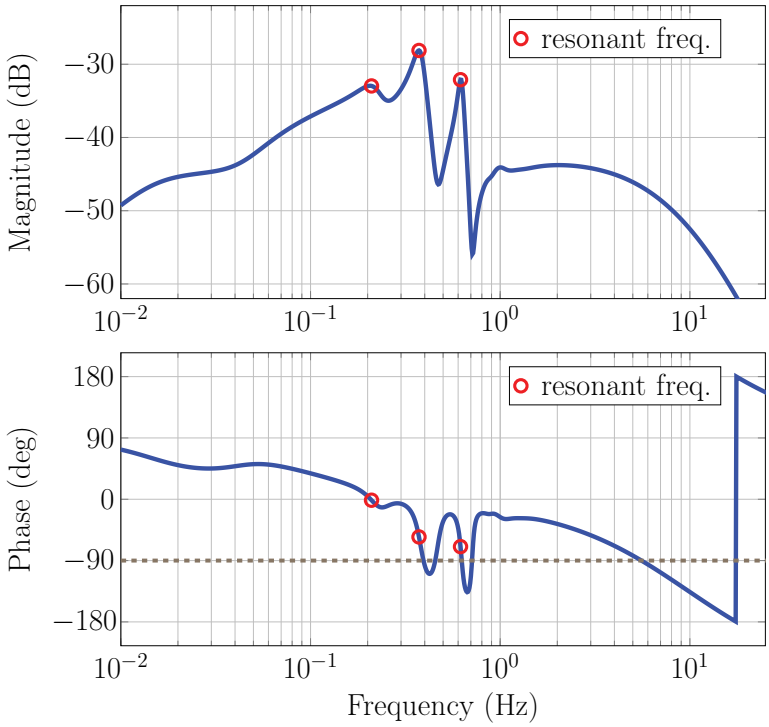

Figure 3.6: The open-loop frequency response between a change in P_{ref} and p_s for the ESS located in British Columbia. At a given frequency, the phase response indicates whether the controller provides damping torque (0°), synchronizing torque (−90°), or some combination thereof.

in the amplitude response. At this frequency, the phase response is roughly 0° indicating that the controller provides more damping torque than synchronizing. At the other two highlighted resonances, the North-South B mode near 0.35 Hz and the British Columbia mode near 0.63 Hz, the phase response is much closer to −90°, indicating a stronger synchronizing response. Although Figure 3.6 corresponds to an individual actuator, these observations mirror the angles of departure shown in Figure 3.5.

3.4 N-1 Contingency Analysis

In this section, we conduct N-1 contingency analysis to study the impact of the control strategy for a range of disturbances. We simulated 28 generator trips, 80 transmission line faults (cleared after 6 cycles), and 19 losses of load (50 % of apparent power). Each contingency was simulated three times: without control, with control, and with control and delays. We employed a statistical communication model that accounts for delays, jitter, and measurement noise. The expected delay for each sensor was uniformly distributed between 67 and 250 ms. The high end of this range is more than double the maximum value reported in a recent real-world experiment [51] (69–113 ms). The actuators were placed and configured as in Section 3.3.1 with a 100 MW ESS located at each of the 19 load centers. Table 3.1 provides a summary of the results. Here the *first swing* of a generator is defined as the magnitude of the initial extremum of $\Delta\delta_i$ following the disturbance. The control strategy reduced the magnitude of 99.4 % of first swings by an average of 14.3 %. For the very small fraction of first swings (0.6 %) that did not decline, the average increase was 1.1 %.

To provide analysis of a representative contingency, we study a 9-cycle fault near generator G34 in Alberta. For this fault, the control strategy improves the critical clearing time from 6 cycles to 10. Figure 3.7 plots the state response in the time-domain, where the upper subplot

Table 3.1: N-1 Contingency Analysis First Swing Summary

Event	First swings (no.)	Improvement rate (%)	Mean decrease in $\Delta\delta$ (%)
Loss of load	646	99.7	18.0
Gen. trip	924	99.5	18.4
Fault/line clearing	2720	99.3	12.1
Total	4290	99.4	14.3

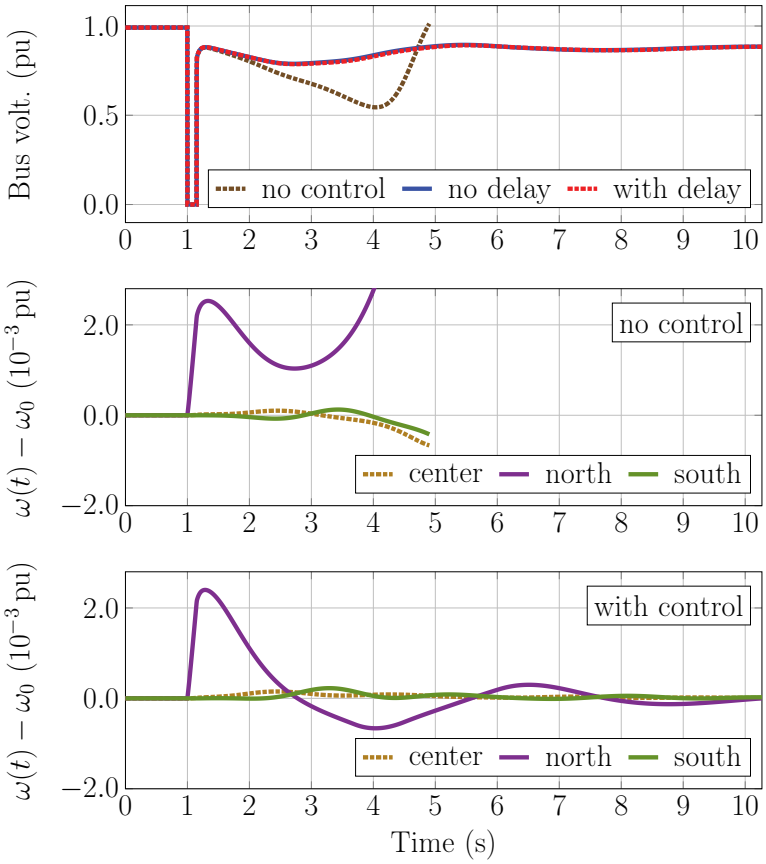

Figure 3.7: Time-domain simulations of a 9-cycle fault near generator G34 in Alberta. The top subplot shows the voltage magnitude at the faulted bus. The bottom two subplots show the LTI speed deviations of G34 in Alberta (north) and G23 in San Diego (south) compared with the center of inertia.

shows the voltage magnitude at the faulted bus. The results with delay overlap those without. The lower subplots show the LTI speed deviations (*i.e.*, $\omega(t) - \omega_0$) for G34 in Alberta, G23 in San Diego, and the center of inertia. Without control, the generator in Alberta loses synchronism. When this occurs, G23 in San Diego begins oscillating against the center of inertia. In practice, out-of-step or overspeed protection would likely trip the critical unit in Alberta before it lost synchronism. This protection may mitigate the oscillations observed

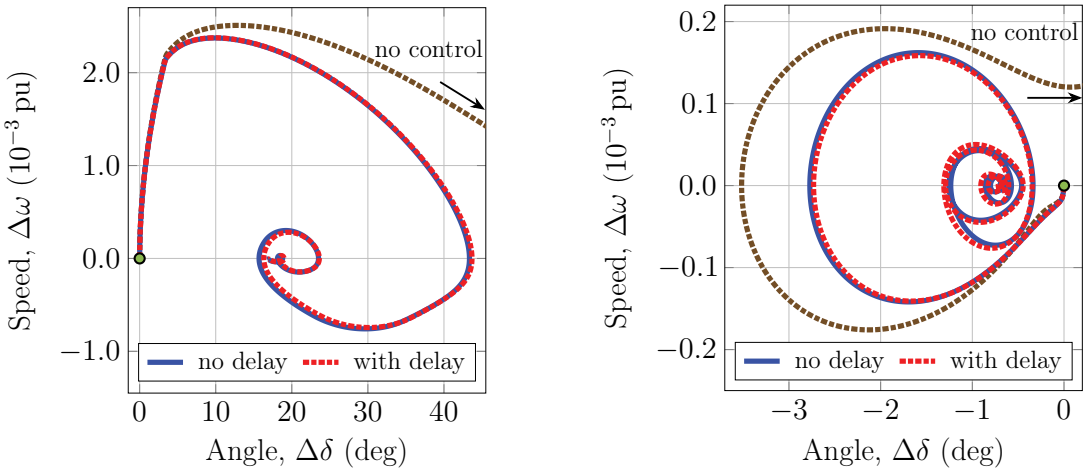

(a) Alberta phase portrait.

(b) San Diego phase portrait.

Figure 3.8: Phase plane analysis in the center-of-inertia reference frame for a 9-cycle fault near generator G34 in Alberta. Subfigure (a) shows the behavior of G34 in Alberta, and (b) G23 in San Diego. All curves begin at the origin.

in San Diego. The bottom subplot shows the speed deviations with control, including the effect of delays and noise. In this case, the generator in Alberta remains synchronized and the oscillations in San Diego subside.

We can gain additional insight into this fault by studying the system response in the angle domain. The phase portraits shown in Figure 3.8 plot the LTV speed deviations $\Delta\omega_i$ versus $\Delta\delta_i$ for the two machines discussed above. Without control, the curves do not arrive at the post-disturbance equilibrium; however, with control, they do. This indicates that the control action expands the region of attraction to encompass the point in the plane where each generator resides immediately after the fault.

Using this perspective, we can also compare the accelerating areas. Under the classical model, the accelerating power of the ith machine in the center-of-inertia reference frame is

$$\Delta P_a^i(t) = P_m^i(t) - P_e^i(t) - \frac{H_i}{H_T}\left[\sum_{k\in\mathcal{K}} P_m^k(t) - P_e^k(t)\right], \tag{3.28}$$

where $\mathcal{K}$ is the set of all online synchronous machines [45]. The top subplot of Figure 3.9

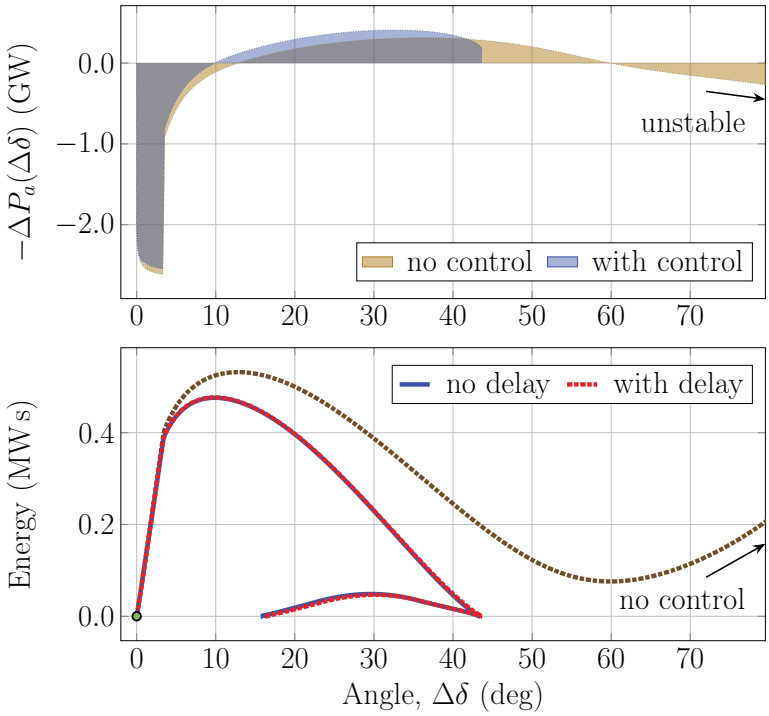

Figure 3.9: Accelerating power analysis in the center-of-inertia reference frame for a 9-cycle fault near generator G34 in Alberta. The top subplot shows the accelerating and decelerating areas with and without control. The bottom subplot shows the integral of accelerating power over $\Delta\delta$.

shows the accelerating power of G34 in Alberta as a function of $\Delta\delta_i$, and the bottom the integral of ΔP_a^i over $\Delta\delta_i$. Assuming the damping constants are negligible, this integral yields the kinetic energy in the center-of-inertia reference frame

$$H_i \Delta\omega_i(t)^2 = \frac{1}{\omega_b} \int_0^{\Delta\delta_i(t)} \Delta P_a^i \, d\Delta\delta_i. \tag{3.29}$$

Without control, the decelerating area is insufficient to cancel the accelerating area, and the machine pulls away from the stable equilibrium. In the bottom subplot, this manifests itself as the failure of the kinetic energy curve to reach the x-axis, *i.e.*, zero energy. The control action reduces the accelerating area and expands the decelerating area, as shown in blue.

This allows the kinetic energy curve to reach the x-axis, where the machine begins its second swing.

In practice, this type of contingency analysis plays an important role in establishing ratings for stability-limited transmission corridors. One such corridor in the Western Interconnection is the California-Oregon Intertie. By choosing a plausible critical contingency for this corridor, we can estimate the impact of the control strategy on the transfer limit. With north-to-south flows, we will assume the critical contingency is a trip of G18 in the miniWECC, a large gas-fired generator near the southern end of the intertie. For this disturbance, we find that the maximum transfer that yields a stable response is 5.3 GW. To determine this limit, we incrementally increased the loading in California and redispatched the generation in the Pacific Northwest. With control, this transfer limit increases to 6.1 GW. Hence, in this example, 1.9 GW of energy storage is able to increase the transfer limit by roughly 800 MW. In reality, this result would need to be confirmed for various operating conditions and multiple critical contingencies.

3.5 Summary

In this chapter, we developed and demonstrated a control strategy that modulates the active power injected by inverter-based resources. The control response was designed to drive the local bus voltage angle toward a trajectory that tracks an estimate of the center-of-inertia angle synthesized from WAMS data. The results in Section 3.4 show that this approach improves system reliability and can increase capacity utilization on stability-limited transmission corridors. Future work will explore techniques and considerations for setpoint management, *i.e.*, when and how to update the constants in (3.24) as the dispatch pattern changes. Finally, another interesting avenue of research will be developing improved hybrid methods for characterizing transient stability margins in nonlinear systems.

Chapter 4
CONCLUSION

In this dissertation, we reassessed traditional approaches to power system stabilization in the context of contemporary measurement and communication technology. The generalized PSS architecture developed in Chapter 2 incorporates local information with a real-time estimate of the speed of the center of inertia. A key feature of this method is that the ability of the stabilizer to improve the damping of electromechanical modes is decoupled from its role in shaping the system response to transient disturbances. Hence, it allows the interaction between the PSS and AVR to be fine-tuned based on voltage requirements. In Chapter 3, we turned our attention to a new method for stabilizing transient disturbances by modulating the active power injected by inverter-based resources. It works in tandem with the generalized PSS architecture, with the PSS designed to produce supplemental damping torque, and the latter method synchronizing torque. The response of the synchronizing controller was designed to drive the local bus voltage angle toward a trajectory that tracks an estimate of the angle of the center of inertia. This approach was observed to improve system reliability and permit increased capacity utilization on stability-limited transmission corridors.

4.1 Key Results

The results showed that the generalized PSS architecture presented in Chapter 2 possesses the following properties:

- It improves the damping of inter-area and local modes of oscillation.
- The ability of the stabilizer to improve damping is decoupled from its role in shaping the system response to transient disturbances.

- The interaction between the PSS and AVR can be precisely adjusted based on voltage requirements.

- The strategy is tolerant of large amounts of delay, especially when $\beta_1 > \beta_2$.

In Chapter 3, we developed a trajectory tracking wide-area synchronizing controller. The properties of this method include:

- The strategy promotes synchronism following large disturbances, such as faults in the transmission system.

- It reduces the need for underfrequency load shedding by supporting the system frequency response (via α_2).

- It can help increase line ratings on stability-limited transmission corridors such as the California-Oregon Intertie.

- The control performance is effectively unchanged for the levels of delay and noise seen in contemporary wide-area measurement systems.

4.2 Suggestions for Future Research

On the basis of the research carried out in this dissertation, problems that merit further investigation include:

- Making the PSS architecture developed in Chapter 2 applicable to a greater number of units by creating a variation that uses integral of accelerating power feedback.

- Obtaining the advantages of a PSS without suppressing voltage by implementing the damping control structure using inverter-based resources.

- Improving the accuracy of wide-area remedial action schemes by redesigning them in the center of inertia reference frame.

- Mitigating the effect of communication and measurement non-idealities by exploring techniques for optimally estimating the speed of the center of inertia.

- Alleviating concerns about the fragility of wide-area measurement systems by developing trajectory tracking strategies that use purely local information.

BIBLIOGRAPHY

[1] IEEE Standard for synchrophasor data transfer for power systems. *IEEE Std C37.118.2-2011*, pages 1–53, December 2011.

[2] IEEE Recommended practice for excitation system models for power system stability studies. *IEEE Std 421.5-2016*, pages 1–207, August 2016.

[3] M. Abdi-Khorsand and V. Vittal. Identification of critical protection functions for transient stability studies. *IEEE Trans. Power Syst.*, 33(3):2940–2948, May 2018.

[4] M. E. Aboul-Ela, A. A. Sallam, J. D. McCalley, and A. A. Fouad. Damping controller design for power system oscillations using global signals. *IEEE Trans. Power Syst.*, 11(2):767–773, May 1996.

[5] P. M. Anderson and B. K. LeReverend. Industry experience with special protection schemes. *IEEE Trans. Power Syst.*, 11(3):1166–1179, August 1996.

[6] T. Athay, R. Podmore, and S. Virmani. A practical method for the direct analysis of transient stability. *IEEE Trans. Power App. Syst.*, PAS-98(2):573–584, March 1979.

[7] A. R. Bergen and D. J. Hill. A structure preserving model for power system stability analysis. *IEEE Trans. Power App. Syst.*, PAS-100(1):25–35, January 1981.

[8] P. Bhui and N. Senroy. Real-time prediction and control of transient stability using transient energy function. *IEEE Trans. Power Syst.*, 32(2):923–934, March 2017.

[9] K. E. Bollinger, R. Winsor, and A. Campbell. Frequency response methods for tuning stabilizers to damp out tie-line power oscillations: Theory and field-test results. *IEEE Trans. Power App. Syst.*, PAS-98(5):1509–1515, September 1979.

[10] J. H. Chow and K. W. Cheung. A toolbox for power system dynamics and control engineering education and research. *IEEE Trans. Power Syst.*, 7(4):1559–1564, November 1992.

[11] J. H. Chow, J. J. Sanchez-Gasca, H. Ren, and S. Wang. Power system damping controller design using multiple input signals. *IEEE Control Syst. Mag.*, 20(4):82–90, August 2000.

[12] S. Ciraci, J. Daily, J. Fuller, A. Fisher, L. Marinovici, and K. Agarwal. FNCS: A framework for power system and communication networks co-simulation. In *Proc. Symp. Theory Model. & Sim. DEVS Int.*, pages 1–8, April 2014.

[13] P. L. Dandeno, A. N. Karas, K. R. McClymont, and W. Watson. Effect of high-speed rectifier excitation systems on generator stability limits. *IEEE Trans. Power App. Syst.*, PAS-87(1):190–201, January 1968.

[14] F. P. Demello and C. Concordia. Concepts of synchronous machine stability as affected by excitation control. *IEEE Trans. Power App. Syst.*, PAS-88(4):316–329, April 1969.

[15] G. J. W. Dudgeon, W. E. Leithead, A. Dyśko, J. O'Reilly, and J. R. McDonald. The effective role of AVR and PSS in power systems: Frequency response analysis. *IEEE Trans. Power Syst.*, 22(4):1986–1994, November 2007.

[16] A. Dyśko, W. E. Leithead, and J. O'Reilly. Enhanced power system stability by coordinated PSS design. *IEEE Trans. Power Syst.*, 25(1):413–422, February 2010.

[17] R. T. Elliott, P. Arabshahi, and D. S. Kirschen. A generalized pss architecture for balancing transient and small-signal response. *IEEE Trans. Power Syst.*, 35(2):1446–1456, March 2020.

[18] R. T. Elliott, A. Ellis, P. Pourbeik, J. J. Sanchez-Gasca, J. Senthil, and J. Weber. Generic photovoltaic system models for WECC–A status report. In *Proc. IEEE Power Energy Soc. Gen. Meeting*, pages 1–5, July 2015.

[19] M. Ghandhari, G. Andersson, and I. A. Hiskens. Control lyapunov functions for controllable series devices. *IEEE Trans. Power Syst.*, 16(4):689–694, November 2001.

[20] E. Gholipour and S. Saadate. Improving of transient stability of power systems using UPFC. *IEEE Trans. Power Del.*, 20(2):1677–1682, April 2005.

[21] M.J. Gibbard, P. Pourbeik, and D.J. Vowles. *Small-signal stability, control and dynamic performance of power systems.* The University of Adelaide Press, 2015.

[22] R. Grondin, I. Kamwa, L. Soulieres, J. Potvin, and R. Champagne. An approach to PSS design for transient stability improvement through supplementary damping of the common low-frequency. *IEEE Trans. Power Syst.*, 8(3):954–963, August 1993.

[23] Y. Guo, D. J. Hill, and Y. Wang. Global transient stability and voltage regulation for power systems. *IEEE Trans. Power Syst.*, 16(4):678–688, November 2001.

[24] M. H. Haque. Evaluation of first swing stability of a large power system with various FACTS devices. *IEEE Trans. Power Syst.*, 23(3):1144–1151, August 2008.

[25] I. A. Hiskens and D. J. Hill. Energy functions, transient stability and voltage behaviour in power systems with nonlinear loads. *IEEE Trans. Power Syst.*, 4(4):1525–1533, November 1989.

[26] K. Hopkinson, X. Wang, R. Giovanini, J. Thorp, K. Birman, and D. Coury. EPOCHS: A platform for agent-based electric power and communication simulation built from commercial off-the-shelf components. *IEEE Trans. Power Syst.*, 21(2):548–558, May 2006.

[27] Hsiao-Dong Chiang, Chia-Chi Chu, and G. Cauley. Direct stability analysis of electric power systems using energy functions: Theory, applications, and perspective. 83(11):1497–1529, November 1995.

[28] IEEE Power & Energy Society. IEEE Tutorial course on power system stabilization via excitation control. Pub. 09TP250. Accessed: June 24, 2019.

[29] I. Kamwa, R. Grondin, and Y. Hebert. Wide-area measurement based stabilizing control of large power systems. *IEEE Trans. Power Syst.*, 16(1):136–153, February 2001.

[30] I. Kamwa, R. Grondin, and G. Trudel. IEEE PSS2B versus PSS4B: The limits of performance of modern power system stabilizers. *IEEE Trans. Power Syst.*, 20(2):903–915, May 2005.

[31] K. Kawabe and A. Yokoyama. Improvement of angle and voltage stability by control of batteries using wide-area measurement system in power systems. In *IEEE Innov. Smart Grid Technol. Europe*, pages 1–7, October 2012.

[32] D. Ke and C. Y. Chung. Design of probabilistically-robust wide-area power system stabilizers to suppress inter-area oscillations of wind integrated power systems. *IEEE Trans. Power Syst.*, 31(6):4297–4309, November 2016.

[33] M. Klein, G. J. Rogers, and P. Kundur. A fundamental study of inter-area oscillations in power systems. *IEEE Trans. Power Syst.*, 6(3):914–921, August 1991.

[34] L. M. Korunović, J. V. Milanović, S. Z. Djokic, K. Yamashita, S. M. Villanueva, and S. Sterpu. Recommended parameter values and ranges of most frequently used static load models. *IEEE Trans. Power Syst.*, 33(6):5923–5934, November 2018.

[35] P. Kundur, N.J. Balu, and M.G. Lauby. *Power system stability and control*. EPRI Power Systems Engineering. McGraw-Hill, 1994.

[36] P. Kundur, M. Klein, G. J. Rogers, and M. S. Zywno. Application of power system stabilizers for enhancement of overall system stability. *IEEE Trans. Power Syst.*, 4(2):614–626, May 1989.

[37] K. T. Law, D. J. Hill, and N. R. Godfrey. Robust controller structure for coordinated power system voltage regulator and stabilizer design. *IEEE Trans. Control Syst. Technol.*, 2(3):220–232, September 1994.

[38] T. Li, G. Ledwich, Y. Mishra, J. H. Chow, and A. Vahidnia. Wave aspect of power system transient stability–Part II: Control implications. *IEEE Trans. Power Syst.*, 32(4):2501–2508, July 2017.

[39] H. Lin, S. Veda, S. Shukla, L. Mili, and J. Thorp. GECO: Global Event-Driven Co-Simulation framework for interconnected power system and communication network. *IEEE Trans. Smart Grid*, 3(3):1444–1456, September 2012.

[40] C. Lu, X. Wu, J. Wu, P. Li, Y. Han, and L. Li. Implementations and experiences of wide-area HVDC damping control in China Southern Power Grid. In *Proc. IEEE Power Energy Soc. Gen. Meeting*, pages 1–7, July 2012.

[41] Y. Ma, L. Zhu, F. Wang, and L. M. Tolbert. Enhancing power system transient stability by virtual synchronous generator control using wide-area measurements. In *IEEE Energy Conv. Congr. and Expo.*, pages 2546–2551, September 2019.

[42] P. C. Magnusson. The transient-energy method of calculating stability. *Trans. AIEE*, 66(1):747–755, January 1947.

[43] Y. Mansour *et al.* BC Hydro's on-line transient stability assessment (TSA) model development, analysis and post-processing. *IEEE Trans. Power Syst.*, 10(1):241–253, February 1995.

[44] G. A. Maria, C. Tang, and J. Kim. Hybrid transient stability analysis. *IEEE Trans. Power Syst.*, 5(2):384–393, May 1990.

[45] A. Michel, A. Fouad, and V. Vittal. Power system transient stability using individual machine energy functions. 30(5):266–276, May 1983.

[46] F. Milano. Rotor speed-free estimation of the frequency of the center of inertia. *IEEE Trans. Power Syst.*, 33(1):1153–1155, January 2018.

[47] B. Naduvathuparambil, M. C. Valenti, and A. Feliachi. Communication delays in wide area measurement systems. In *Proc. 34th Southeastern Symp. on Syst. Theory*, pages 118–122, March 2002.

[48] M. A. Pai. *Energy Function Analysis for Power System Stability*. Power Electronics and Power Systems. Springer US, 1989.

[49] B. Palmintier, D. Krishnamurthy, P. Top, S. Smith, J. Daily, and J. Fuller. Design of the HELICS high-performance transmission-distribution-communication-market co-simulation framework. In *Proc. Model. Sim. Cyber-Phys. Energy Syst.*, pages 1–6, April 2017.

[50] B. Pierre, R. Elliott, D. Schoenwald, J. Neely, R. Byrne, D. Trudnowski, and J. Colwell. Supervisory system for a wide area damping controller using PDCI modulation and real-time PMU feedback. In *Proc. IEEE Power Energy Soc. Gen. Meeting*, pages 1–5, July 2016.

[51] B. J. Pierre, F. Wilches-Bernal, D. A. Schoenwald, R. T. Elliott, D. J. Trudnowski, R. H. Byrne, and J. C. Neely. Design of the Pacific DC Intertie wide area damping controller. *IEEE Trans. Power Syst.*, 34(5):3594–3604, September 2019.

[52] H. Quinot, H. Bourlès, and T. Margotin. Robust coordinated AVR+PSS for damping large-scale power systems. *IEEE Trans. Power Syst.*, 14(4):1446–1451, November 1999.

[53] G. F. Riley and T. R. Henderson. *The ns-3 Network Simulator*, chapter I, pages 15–34. Springer Berlin Heidelberg, Berlin, Heidelberg, 2010.

[54] G. Rogers. *Power system oscillations*. Power Electronics and Power Systems. Kluwer Academic Publishers, 1999.

[55] M. Rylander, W. M. Grady, A. Arapostathis, and E. J. Powers. Power electronic transient load model for use in stability studies of electric power grids. *IEEE Trans. Power Syst.*, 25(2):914–921, May 2010.

[56] S. E. Stanton, C. Slivinsky, K. Martin, and J. Nordstrom. Application of phasor measurements and partial energy analysis in stabilizing large disturbances. *IEEE Trans. Power Syst.*, 10(1):297–306, February 1995.

[57] C. J. Távora and O. J. M. Smith. Characterization of equilibrium and stability in power systems. *IEEE Trans. Power App. Syst.*, PAS-91(3):1127–1130, May 1972.

[58] D. Trudnowski, D. Kosterev, and J. Undrill. PDCI damping control analysis for the western North American power system. In *Proc. IEEE Power Energy Soc. Gen. Meeting*, pages 1–5, July 2013.

[59] D. Trudnowski, D. Kosterev, and J. Wold. Open-loop PDCI probing tests for the western North American power system. In *Proc. IEEE Power Energy Soc. Gen. Meeting*, pages 1–5, July 2014.

[60] K. Uhlen, L. Vanfretti, M. M. de Oliveira, A. B. Leirbukt, V. H. Aarstrand, and J. O. Gjerde. Wide-area power oscillation damper implementation and testing in the Norwegian transmission network. In *Proc. IEEE Power Energy Soc. Gen. Meeting*, pages 1–7, July 2012.

[61] A. Ulbig, T. S. Borsche, and G. Andersson. Impact of low rotational inertia on power system stability and operation. In *Proc. 19th IFAC World Congr.*, pages 7290–7297, August 2014.

[62] U.S. Energy Information Administration. Annual energy outlook 2019 with projections to 2050. EIA/AEO2019. Accessed: July 1, 2019.

[63] P. Varaiya, F. F. Wu, and Rong-Liang Chen. Direct methods for transient stability analysis of power systems: Recent results. 73(12):1703–1715, December 1985.

[64] V. Vittal. *Power system transient stability using the critical energy of individual machines.* Retrospective theses and dissertations, Iowa State University, 1982.

[65] Y. Wang, D. J. Hill, R. H. Middleton, and L. Gao. Transient stability enhancement and voltage regulation of power systems. *IEEE Trans. Power Syst.*, 8(2):620–627, May 1993.

[66] Western Electric Coordinating Council. WECC policy statement: Power system stabilizers. Accessed: Sep. 11, 2017.

[67] F. Wilches-Bernal, J. H. Chow, and J. J. Sanchez-Gasca. A fundamental study of applying wind turbines for power system frequency control. *IEEE Trans. Power Syst.*, 31(2):1496–1505, March 2016.

[68] F. Wilches-Bernal, R. Concepcion, J. C. Neely, D. A. Schoenwald, R. H. Byrne, B. J. Pierre, and R. T. Elliott. Effect of time delay asymmetries in power system damping control. In *Proc. IEEE Power Energy Soc. Gen. Meeting*, pages 1–5, July 2017.

[69] F. Wilches-Bernal, B. J. Pierre, R. T. Elliott, D. A. Schoenwald, R. H. Byrne, J. C. Neely, and D. J. Trudnowski. Time delay definitions and characterization in the Pacific DC Intertie wide area damping controller. In *Proc. IEEE Power Energy Soc. Gen. Meeting*, pages 1–5, July 2017.

[70] F. Wilches-Bernal, D. A. Schoenwald, R. Fan, M. Elizondo, and H. Kirkham. Analysis of the effect of communication latencies on HVDC-based damping control. In *Proc. IEEE PES Tran. Dist. Conf. Expo.*, pages 1–9, April 2018.

[71] H. Wu, K. S. Tsakalis, and G. T. Heydt. Evaluation of time delay effects to wide-area power system stabilizer design. *IEEE Trans. Power Syst.*, 19(4):1935–1941, November 2004.

[72] Y. Xue, T. Van Custem, and M. Ribbens-Pavella. Extended equal area criterion justifications, generalizations, applications. *IEEE Trans. Power Syst.*, 4(1):44–52, February 1989.

[73] Z. Yao. A control-oriented energy function for generation shedding determination for transient stability control. *IEEE Trans. Power Syst.*, 34(1):413–421, January 2019.

[74] R. Yousefian, R. Bhattarai, and S. Kamalasadan. Transient stability enhancement of power grid with integrated wide area control of wind farms and synchronous generators. *IEEE Trans. Power Syst.*, 32(6):4818–4831, November 2017.

[75] J. Zaborszky, K. Prasad, and Keh-Wen Whang. Stabilizing control in emergencies–Part 2: Control by local feedback. *IEEE Trans. Power App. Syst.*, PAS-100(5):2381–2389, May 1981.

[76] S. Zhang and V. Vittal. Design of wide-area power system damping controllers resilient to communication failures. *IEEE Trans. Power Syst.*, 28(4):4292–4300, November 2013.

[77] S. Zhang and V. Vittal. Wide-area control resiliency using redundant communication paths. *IEEE Trans. Power Syst.*, 29(5):2189–2199, September 2014.

[78] G. C. Zweigle and V. Venkatasubramanian. Wide-area optimal control of electric power systems with application to transient stability for higher order contingencies. *IEEE Trans. Power Syst.*, 28(3):2313–2320, August 2013.

Appendix A

MAP OF THE MINIWECC

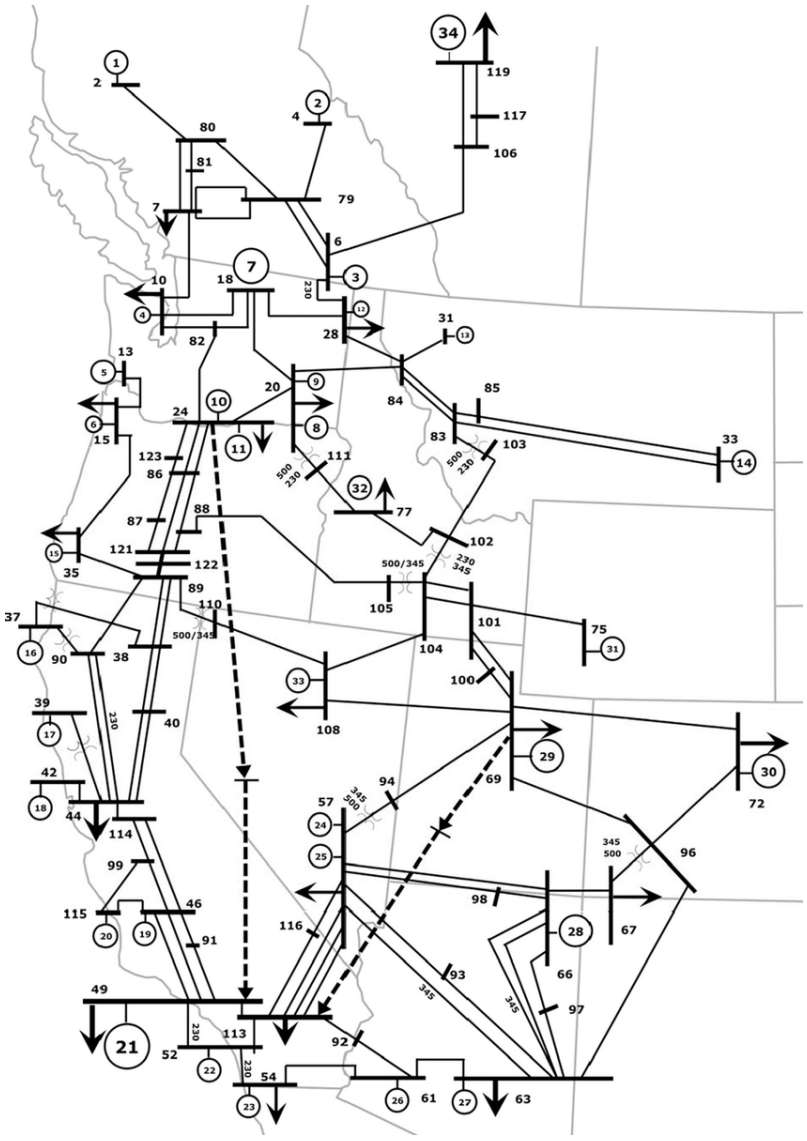

Figure A.1: Oneline diagram of the miniWECC overlaid on a map.

Appendix B

DYNAMIC MODEL CODE ACCOMPANYING CHAPTER 2

```
function [f] = pss(i,k,bus,flag)

% Syntax: [f] = pss(i,k,bus,flag)
%
% Purpose: wide-area power system stabilization model
%
% Input: i - generator number
%        k - integer time
%        bus - solved loadflow bus data
%        flag - 0 - initialization
%               1 - network interface computation
%               2 - system dynamics computation
%
% Output: f - dummy variable
%
% Wide-area PSS implementation
% Version:  0.1
% Author:   Ryan T. Elliott
% Date:     November 2017

global  pss_con pss_pot pss_mb_idx pss_exc_idx
global  pss1 pss2 pss3 dpss1 dpss2 dpss3 pss_out
global  pss_idx n_pss pss_sp_idx pss_p_idx pss_wa_idx
global  pss_T pss_T2 pss_T4 pss_T4_idx pss_noT4_idx
global  dpw_pss_idx n_dpw dpw_out
global  sw_con mac_con mac_int mac_spd pelect basmva
global  my_waref

%-------------------------------------------------------------------------%

f = 0;
if (n_pss ~= 0)
    if (i ~= 0)
        if (pss_con(i,1) ~= 1 && pss_con(i,1) ~= 2 && pss_con(i,1) ~= 3)
            error('PSS: inappropriate power system stablizer model')
        end
```

```
end

jay = sqrt(-1);
num_mac = length(mac_con(:,1));

if (flag == 0)                          % initialization
    if (i ~= 0)                         % scalar computation
        n = pss_mb_idx(i);              % machine number
        if (pss_con(i,1) == 1)
            pss1(i,1) = mac_spd(n,1);
        elseif (pss_con(i,1) == 2)
            pss1(i,1) = pelect(n,1)*basmva/mac_con(n,3);
        else                            % wide-area PSS
            pss1(i,1) = 0;
        end

        if n_dpw ~= 0
            i_dpw = find(dpw_pss_idx==i);
            if ~isempty(i_dpw)
                pss1(i,1) = dpw_out(i_dpw,1);
            end
        end

        pss2(i,1) = 0.;
        pss3(i,1) = 0.;
        pss_out(pss_exc_idx(i),1) = 0.0;
        pss_pot(i,1) = pss_con(i,5)/pss_con(i,6);
        pss_pot(i,2) = 1.0;

        if (pss_con(i,8) ~= 0)
            pss_pot(i,2) = pss_con(i,7)/pss_con(i,8);
        end
    else

        % vector computation
        pss_pot = ones(n_pss,2);
        n = pss_mb_idx;

        if ~isempty(pss_sp_idx)
            n_sp = mac_int(pss_con(pss_sp_idx,2));
            pss1(pss_sp_idx,1) = mac_spd(n_sp,1);
        end

        if ~isempty(pss_wa_idx)         % wide-area PSS
```

```
            n_wa = mac_int(pss_con(pss_wa_idx,2));
            pss1(pss_wa_idx,1) = 0;
        end

        if ~isempty(pss_p_idx)
            n_p = mac_int(pss_con(pss_p_idx,2));
            pss1(pss_p_idx,1) = pelect(n_p,1)*basmva./mac_con(n_p,3);
        end

        if (n_dpw ~= 0)
            pss1(dpw_pss_idx,1) = dpw_out(:,1);
        end

        pss2(pss_idx,1) = zeros(n_pss,1);
        pss3(pss_idx,1) = zeros(n_pss,1);
        pss_out(pss_exc_idx,1) = zeros(n_pss,1);
        pss_pot(:,1) = pss_con(:,5)./pss_con(:,6);


        if ~isempty(pss_T4_idx)
            pss_pot(pss_T4_idx,2) = ...
            pss_con(pss_T4_idx,7)./pss_T4(pss_T4_idx);
        end
    end
end

if (flag == 1)                          % network interface computation
    if (i ~= 0)                         % scalar computation
        n = pss_mb_idx(i);              % machine number
        if (pss_con(i,1) == 1)
            var1 = (mac_spd(i,k)-pss1(i,k))/pss_con(i,4);
        elseif (pss_con(i,1) == 2)
            n = mac_int(pss_con(i,2));  % machine number
            var1_tmp = pelect(i,k)*basmva/mac_con(n,3) - pss1(i,k);
            var1 = var1_tmp/pss_con(i,4);
        else                            % wide-area PSS
            var1 = (my_Kwa*(mac_spd(i,k) - my_waref(k))...
                    + my_Kcm*(my_waref(k) - 1) - pss1(i,k))/pss_con(i,4);
        end

        if (n_dpw ~= 0)
            if (n_dpw ~= 0)
                i_dpw = find(dpw_pss_idx==i);
                if ~isempty(i_dpw)
```

```
                var1 = (dpw_out(i_dpw,k)-pss1(i,k))/pss_con(i,4);
            end
        end
    end

    var2 = pss_pot(i,1)*pss_con(i,3)*var1 + pss2(i,k);

    if pss_con(i,8) == 0
        var3 = var2;
    else
        var3 = pss_pot(i,2)*var2 + pss3(i,k);
    end

    pss_out(pss_exc_idx(i),k) = ...
        min(pss_con(i,9),max(var3,-pss_con(i,9)));
else
    % vector computation
    if (n_pss ~= 0)
        n = pss_mb_idx;             % machine number vector

        var1 = zeros(n_pss,1);
        var2 = var1; var3 = var1;
        if ~isempty(pss_sp_idx)
            n_sp = mac_int(pss_con(pss_sp_idx,2));

            var1_tmp = mac_spd(n_sp,k) - pss1(pss_sp_idx,k);
            var1(pss_sp_idx) = var1_tmp./pss_con(pss_sp_idx,4);
        end

        if ~isempty(pss_wa_idx)     % wide-area PSS
            n_wa = mac_int(pss_con(pss_wa_idx,2));
            var1_tmp = (my_Kwa*(mac_spd(n_wa,k) - my_waref(k))...
                     + my_Kcm*(my_waref(k) - 1) - pss1(pss_wa_idx,k));
            var1(pss_wa_idx) = var1_tmp./pss_con(pss_wa_idx,4);
        end

        if ~isempty(pss_p_idx)
            n_p = mac_int(pss_con(pss_p_idx,2));
            var1_tmp = pelect(n_p,k)*basmva./mac_con(n_p,3)...
                       - pss1(pss_p_idx,k);
            var1(pss_p_idx) = var1_tmp./pss_con(pss_p_idx,4);
        end

        if (n_dpw ~= 0)
```

```
                var1_tmp = dpw_out(:,k) - pss1(dpw_pss_idx,k);
                var1 = var1_tmp./pss_con(dpw_pss_idx,4);
            end
        end

        var2(pss_idx) = pss_pot(pss_idx,1).*(pss_con(pss_idx,3).*var1)...
                        + pss2(pss_idx,k);
        var3 = var2;

        if ~isempty(pss_T4_idx)
            var3_tmp = pss_pot(pss_T4_idx,2).*var2(pss_T4_idx,1);
            var3(pss_T4_idx,1) = var3_tmp + pss3(pss_T4_idx,k);
        end

        pss_out(pss_exc_idx,k) = ...
            min(pss_con(pss_idx,9),max(var3,pss_con(pss_idx,10)));
    end
end

if (flag == 2)                          % pss dynamics calculation
    if (i ~= 0)                         % scalar computation
        n = pss_mb_idx(i);              % machine number
        if (pss_con(i,1) == 1)
            var1 = (mac_spd(i,k) - pss1(i,k))/pss_con(i,4);
        elseif (pss_con(i,1) == 2)
            n = mac_int(pss_con(i,2));  % machine number
            var1_tmp = pelect(i,k)*basmva./mac_con(n,3) - pss1(i,k);
            var1 = var1_tmp/pss_con(i,4);
        else                            % wide-area PSS
            var1 = (my_Kwa*(mac_spd(i,k) - my_waref(k))...
                    + my_Kcm*(my_waref(k) - 1) - pss1(i,k))/pss_con(i,4);
        end

        if (n_dpw ~= 0)
            if (n_dpw ~= 0)
                i_dpw = find(dpw_pss_idx==i);
                if ~isempty(i_dpw)
                    var1 = (dpw_out(i_dpw,k)-pss1(i,k))/pss_con(i,4);
                end
            end
        end

        dpss1(i,k) = var1;
```

```
    var2 = pss_pot(i,1)*pss_con(i,3)*var1 + pss2(i,k);
    dpss2(i,k) = ...
        ((1-pss_pot(i,1))*pss_con(i,3)*var1 - pss2(i,k))/pss_con(i,6);

    if pss_con(i,8) == 0
        var3 = var2;
        dpss3(i,k) = dpss2(i,k);
    else
        var3 = pss_pot(i,2)*var2 + pss3(i,k);
        dpss3(i,k) = ((1-pss_pot(i,2))*var2 - pss3(i,k))/pss_con(i,8);
    end

    pss_out(pss_exc_idx(i),k) = ...
        min(pss_con(i,9),max(var3,-pss_con(i,9)));

else

    % vector computation
    if (n_pss ~= 0)
        n = pss_mb_idx;             % machine number vector
        var1 = zeros(n_pss,1);
        var2 = var1; var3 = var1;
        if ~isempty(pss_sp_idx)
            n_sp = mac_int(pss_con(pss_sp_idx,2));
            var1(pss_sp_idx) = (mac_spd(n_sp,k)-pss1(pss_sp_idx,k))...
                               ./pss_con(pss_sp_idx,4);
        end

        if ~isempty(pss_wa_idx)     % wide-area PSS
            n_wa = mac_int(pss_con(pss_wa_idx,2));
            var1_tmp = (my_Kwa*(mac_spd(n_wa,k) - my_waref(k))...
                     + my_Kcm*(my_waref(k) - 1) - pss1(pss_wa_idx,k));
            var1(pss_wa_idx) = var1_tmp./pss_con(pss_wa_idx,4);
        end

        if ~isempty(pss_p_idx)
            n_p = mac_int(pss_con(pss_p_idx,2));
            var1_tmp = (pelect(n_p,k)*basmva./mac_con(n_p,3)...
                        - pss1(pss_p_idx,k));
            var1(pss_p_idx) = var1_tmp./pss_con(pss_p_idx,4);
        end

        if (n_dpw ~= 0)
            var1_tmp = (dpw_out(:,k)-pss1(dpw_pss_idx,k));
```

```
                var1 = var1_tmp./pss_con(dpw_pss_idx,4);
            end
        end

        dpss1(pss_idx,k) = var1;

        var2 = pss_pot(pss_idx,1).*(pss_con(pss_idx,3).*var1)...
               + pss2(pss_idx,k);
        dpss2(pss_idx,k) = ((ones(n_pss,1)-pss_pot(pss_idx,1))...
                            .*(pss_con(pss_idx,3).*var1)...
                            - pss2(pss_idx,k))./pss_con(pss_idx,6);

        var3 = var2;
        dpss3(:,k) = dpss2(:,k);
        if ~isempty(pss_T4_idx)
            var3(pss_T4_idx) = pss_pot(pss_T4_idx,2).*var2(pss_T4_idx)...
                               + pss3(pss_T4_idx,k);
            dpss3(pss_T4_idx,k) = ((ones(length(pss_T4_idx),1)...
                            - pss_pot(pss_T4_idx,2)).*var2(pss_T4_idx)...
                            - pss3(pss_T4_idx,k))./pss_T4(pss_T4_idx);
        end

        pss_out(pss_exc_idx,k) =...
            min(pss_con(pss_idx,9),max(var3,pss_con(pss_idx,10)));
    end
  end
end

end  % function end

% eof
```

Appendix C

DYNAMIC MODEL CODE ACCOMPANYING CHAPTER 3

```
function f = ess(i,k,bus,vnc_ess,flag)

% Syntax: f = ess(i,k,bus,vnc_ess,flag)
% 08/13/2019
%
% Purpose: energy storage system,
%          with vectorized computation option
%          NOTE - energy storage buses must be declared as a
%                 non-conforming load bus
% Input: i - energy storage system number (index)
%            if i = 0, vectorized computation
%        k - integer time
%        bus - solved loadflow bus data
%        vnc_ess - voltage at nc_load buses for flag == 4
%               pass vnc_ess = nan for other cases
%        flag - 0 - initialization
%               1 - network interface computation
%               2 - generator dynamics computation
%               3 - iterative network interface computation (for nc_load)
%
% Output: f - a dummy variable
%
% ess_con matrix format
% col   data                                          units
%  1    energy storage system/converter number       integer
%  2    bus number                                   integer
%  3    use Pade approximants flag (0 = bypass)      binary
%  4    remote signal time delay (Pade)              sec
%  5    local signal time delay (Pade)               sec
%  6    voltage transducer time constant             sec
%  7    remote angle setpoint rate limit             pu
%  8    remote angle setpoint time constant          sec
%  9    local angle setpoint rate limit              pu
% 10    local angle setpoint time constant           sec
% 11    local LTV tuning weight (alpha 1)            pu
% 12    local LTV highpass numerator 1               sec
```

```
% 13    local LTV highpass numerator 2              sec
% 14    local LTV highpass denominator 1            sec
% 15    local LTV highpass denominator 2            sec
% 16    local LTV lead-lag stage 1 numerator        sec
% 17    local LTV lead-lag stage 1 denominator      sec
% 18    local LTV lead-lag stage 2 numerator        sec
% 19    local LTV lead-lag stage 2 denominator      sec
% 20    local LTV modulation command minimum        pu
% 21    local LTV modulation command maximum        pu
% 22    center LTI tuning weight (alpha 2)          pu
% 23    center LTI highpass numerator 1             sec
% 24    center LTI highpass numerator 2             sec
% 25    center LTI highpass denominator 1           sec
% 26    center LTI highpass denominator 2           sec
% 27    center LTI lead-lag stage 1 numerator       sec
% 28    center LTI lead-lag stage 1 denominator     sec
% 29    center LTI lead-lag stage 2 numerator       sec
% 30    center LTI lead-lag stage 2 denominator     sec
% 31    center LTI modulation command minimum       pu
% 32    center LTI modulation command maximum       pu
% 33    transient stability control gain            pu
% 34    lowpass filter time constant                sec
% 35    total modulation command minimum            pu
% 36    total modulation command maximum            pu
% 37    power capacity                              MW
% 38    energy capacity                             MWh
% 39    initial power injection                     pu
% 40    initial state of charge                     pu
% 41    minimum state of charge                     pu
% 42    maximum state of charge                     pu
% 43    active current ramp rate limit              pu
% 44    converter interface time constant           sec
% 45    charge/discharge only indicator             integer
%           1 = charge only; 2 = discharge only     --
% 46    charge/discharge efficiency                 pu
%
% ess_pot matrix format
% col   data                          units
%  1    power capacity                pu on system base
%  2    energy base conversion factor pu/sec on ess base
%
% ess states
% var    description
% ess1   transducer for remote angle signal
```

```
% ess2   transducer for local angle signal
% ess3   transducer for local voltage magnitude
% ess4   Pade approx. for remote angle signal
% ess5   Pade approx. for local angle signal
% ess6   Pade approx. for local voltage magnitude
% ess7   remote angle signal setpoint tracking filter
% ess8   local angle signal setpoint tracking filter
% ess9   local LTV highpass filter state 1
% ess10  local LTV highpass filter state 2
% ess11  local LTV lead-lag stage 1
% ess12  local LTV lead-lag stage 2
% ess13  center LTI highpass filter state 1
% ess14  center LTI highpass filter state 2
% ess15  center LTI lead-lag stage 1
% ess16  center LTI lead-lag stage 2
% ess17  lowpass filter
% ess18  active current converter interface
% ess19  reactive current converter interface
% ess20  state of charge integrator
%
% (c) Copyright 2019 Ryan Elliott, University of Washington
%     All Rights Reserved
%-------------------------------------------------------------------------------%

% system variables
global basmva bus_int mac_con mac_ang

% ess variables
global ess_con ess_pot ess_idx n_ess ess_del
global ess_cur ess_sinj ess_soc ess_vmag ess_vmag_pade ess_pcmd ess_ip_ord
global theta_ess theta_coi theta_coi_del theta_err theta_ess_pade theta_coi_pade
global bus_v bus_nomac int_nomac
global ess_sig ess_dsig

% state variables and derivatives
global ess1 ess2 ess3 ess4 ess5 ess6 ess7 ess8 ess9 ess10
global ess11 ess12 ess13 ess14 ess15 ess16 ess17 ess18 ess19 ess20
global dess1 dess2 dess3 dess4 dess5 dess6 dess7 dess8 dess9 dess10
global dess11 dess12 dess13 dess14 dess15 dess16 dess17 dess18 dess19 dess20

%-------------------------------------------------------------------------------%

lbnd = 1e-3;                    % lower bound to prevent division by zero
int_nomac = bus_int(bus_nomac);  % internal buses with no synchronous machines
```

```
sensor_set = int_nomac(1:3:end); % no generator buses
n_sensor = length(sensor_set);   % ~36 sensors for miniWECC

i_lvpl1 = 1.22*ones(n_ess,1);    % LVPL breakpoint current (pu)
v_zerox = 0.4*ones(n_ess,1);     % LVPL zero crossing
v_break = 0.9*ones(n_ess,1);     % LVPL breakpoint voltage (pu)

f = 0;
if ~isempty(ess_con)
    if (flag == 0)               % initialization
        if (i ~= 0)
              % NOTE: Non-vectorized computation is not supported!
        else  % vectorized calculation (initialization)

            busnum = bus_int(ess_con(:,2));              % bus number vector

            ess_con(:,39) = -bus(busnum,6);              % initial power inj.
            ess_vmag(:,1) = bus(busnum,2);               % ess bus volt.
            theta_ess(:,1) = bus(busnum,3)*pi/180;       % ess bus volt. ang.
            theta_ess_pade(:,1) = theta_ess(:,1);        % delayed angle

            theta_coi(:,1) = sum(bus(sensor_set,3)*pi/180)/n_sensor;
            theta_err(:,1) = theta_ess(:,1) - theta_coi(:,1);

            ess_sinj(:,1) = -(bus(busnum,6) + 1j*bus(busnum,7)*0);
          % ess_sinj(:,1) = -(bus(busnum,6) + 1j*bus(busnum,7));
            ip_inj = real(ess_sinj(:,1)./max(ess_vmag(:,1),lbnd));
          % iq_inj = imag(ess_sinj(:,1)./max(ess_vmag(:,1),lbnd));
            ess_soc(:,1) = ess_con(:,40);                % ess soc

            ess_pot(:,1) = ess_con(:,37)/basmva;         % power capacity
            ess_pot(:,2) = basmva./(ess_con(:,38)*3600); % base conversion

            ess1(:,1) = theta_coi(:,1);  % transducer for remote angle
            ess2(:,1) = theta_ess(:,1);  % transducer for local angle
            ess3(:,1) = ess_vmag(:,1);   % transducer for local voltage
            ess4(:,1) = theta_coi(:,1);  % Pade approx. for remote angle
            ess5(:,1) = theta_ess(:,1);  % Pade approx. for local angle
            ess6(:,1) = ess_vmag(:,1);   % Pade approx. for local voltage
            ess7(:,1) = theta_coi(:,1);  % remote angle signal setpoint
            ess8(:,1) = theta_ess(:,1);  % local angle signal setpoint
            ess9(:,1) = 0.0;             % local LTV highpass filter state 1
            ess10(:,1) = 0.0;            % local LTV highpass filter state 2
            ess11(:,1) = 0.0;            % local LTV lead-lag stage 1
```

```
ess12(:,1) = 0.0;            % local LTV lead-lag stage 2
ess13(:,1) = 0.0;            % center LTI highpass filter state 1
ess14(:,1) = 0.0;            % center LTI highpass filter state 2
ess15(:,1) = 0.0;            % center LTI lead-lag stage 1
ess16(:,1) = 0.0;            % center LTI lead-lag stage 2
ess17(:,1) = 0.0;            % lowpass filter
ess18(:,1) = ip_inj;         % active current converter interface
ess19(:,1) = 0.0;            % reactive current converter interface
ess20(:,1) = 0.0;            % state of charge integrator

dess1(:,1) = 0.0;
dess2(:,1) = 0.0;
dess3(:,1) = 0.0;
dess4(:,1) = 0.0;
dess5(:,1) = 0.0;
dess6(:,1) = 0.0;
dess7(:,1) = 0.0;
dess8(:,1) = 0.0;
dess9(:,1) = 0.0;
dess10(:,1) = 0.0;
dess11(:,1) = 0.0;
dess12(:,1) = 0.0;
dess13(:,1) = 0.0;
dess14(:,1) = 0.0;
dess15(:,1) = 0.0;
dess16(:,1) = 0.0;
dess17(:,1) = 0.0;
dess18(:,1) = 0.0;
dess19(:,1) = 0.0;
dess20(:,1) = 0.0;

mask = (ess_con(:,20) >= ess_con(:,21));
if any(mask)
    estr = 'ESS: Impermissible local LTV modulation limits at ';
    estr = [estr, 'bus %0.0f, min >= max.\n'];
    error(estr, busnum(mask));
end

mask = (ess_con(:,31) >= ess_con(:,32));
if any(mask)
    estr = 'ESS: Impermissible center LTI modulation limits at ';
    estr = [estr, 'bus %0.0f, min >= max.\n'];
    error(estr, busnum(mask));
end
```

```
        mask = (ess_con(:,35) >= ess_con(:,36));
        if any(mask)
            estr = 'ESS: Impermissible total modulation limits at ';
            estr = [estr, 'bus %0.0f, min >= max.\n'];
            error(estr, busnum(mask));
        end

        mask = (ess_con(:,40) < ess_con(:,41));
        if any(mask)
            estr = 'ESS: SOC below minimum at initialization at ';
            estr = [estr, 'bus %0.0f.\n'];
            error(estr, busnum(mask));
        end

        mask = (ess_con(:,40) > ess_con(:,42));
        if any(mask)
            estr = 'ESS: SOC exceeds maximum at initialization at ';
            estr = [estr, 'bus %0.0f.\n'];
            error(estr, busnum(mask));
        end

        mask = (ess_con(:,41) >= ess_con(:,42));
        if any(mask)
            estr = 'ESS: Impermissible SOC limits at ';
            estr = [estr, 'bus %0.0f, min >= max.\n'];
            error(estr, busnum(mask));
        end

        mask = (abs(ess_sinj(:,1)) > ess_pot(:,1));
        if any(mask)
            estr = 'ESS: Power exceeds maximum at initialization at ';
            estr = [estr, 'bus %0.0f.\n'];
            error(estr, busnum(mask));
        end
    end
end

if (flag == 1)  % network interface computation
    % iterative interface calculation required - done in flag == 4
end

if (flag == 2 || flag == 3)  % dynamics calculation
    if (i ~= 0)
```

```
      % NOTE: Non-vectorized computation is not supported!
else  % vectorized computation (dynamics calculation)

    busnum = bus_int(ess_con(:,2));           % ess bus number vector

    ess_vmag(:,k) = abs(bus_v(busnum,k));     % ess bus voltage mag
    theta_ess_tmp = angle(bus_v(busnum,k));   % ess bus voltage angle
    theta_coi_tmp = sum(angle(bus_v(sensor_set,k)));

    angle_jump_pmu = angle(bus_v(sensor_set,k))...
                       - angle(bus_v(sensor_set,max(1,k-1)));
    fault_flag = (max(abs(angle_jump_pmu)) < pi) ...
                  && (abs(sum(angle_jump_pmu)) > pi);

    angle_jump_ess = theta_ess_tmp - theta_ess(:,max(1,k-1));
    angle_jump_ess = ess_unwrap(angle_jump_ess, 0);

    angle_jump_coi = theta_coi_tmp - n_sensor*theta_coi(:,max(1,k-1));
    angle_jump_coi = ess_unwrap(angle_jump_coi, fault_flag);

    theta_ess(:,k) = theta_ess(:,max(1,k-1)) + angle_jump_ess;

    coi_num_tmp = (n_sensor*theta_coi(:,max(1,k-1)) + angle_jump_coi);
    theta_coi(:,k) = coi_num_tmp/n_sensor;

    %-----------------------------------------------------------------%
    % voltage magnitude and angle transducers

    theta_coi_del(:,k) = theta_coi(:,k);

    dess1_tmp = theta_coi_del(:,k) - ess1(:,k);
    dess1(:,k) = dess1_tmp./max(ess_con(:,6),lbnd);
    dess2(:,k) = (theta_ess(:,k) - ess2(:,k))./max(ess_con(:,6),lbnd);
    dess3(:,k) = (ess_vmag(:,k) - ess3(:,k))./max(ess_con(:,6),lbnd);

    mask = (ess_con(:,6) < lbnd);
    if any(mask)                              % integrator bypass
        dess1(mask,k) = 0.0;
        dess2(mask,k) = 0.0;
        dess3(mask,k) = 0.0;

        ess1(mask,k) = theta_coi_del(mask,k);  % center-of-inertia ang.
        ess2(mask,k) = theta_ess(mask,k);      % local voltage ang.
        ess3(mask,k) = ess_vmag(mask,k);       % local voltage mag.
```

```
end

%-------------------------------------------------------------------%
% time delay via Pade approximants

% u_remote_pade = ess1(:,k);               % remote angle meas.

dess4(:,k) = (ess1(:,k) - ess4(:,k))./max(ess_con(:,4)/2,lbnd);

mask = (ess_con(:,4)/2 < lbnd);
if any(mask)                               % integrator bypass
    dess4(mask,k) = 0.0;
    ess4(mask,k) = ess1(mask,k);           % average voltage angle
end

theta_coi_pade(:,k) = 2*ess4(:,k) - ess1(:,k);

% u_local_pade = ess2(:,k);                % local angle meas.
% u_volt_pade = ess3(:,k);                 % local voltage mag.

dess5(:,k) = (ess2(:,k) - ess5(:,k))./max(ess_con(:,5)/2,lbnd);
dess6(:,k) = (ess3(:,k) - ess6(:,k))./max(ess_con(:,5)/2,lbnd);

mask = (ess_con(:,5)/2 < lbnd);
if any(mask)                               % integrator bypass
    dess5(mask,k) = 0.0;
    dess6(mask,k) = 0.0;

    ess5(mask,k) = ess2(mask,k);           % local voltage ang.
    ess6(mask,k) = ess3(mask,k);           % local voltage mag.
end

theta_ess_pade(:,k) = 2*ess5(:,k) - ess2(:,k);
ess_vmag_pade(:,k) = 2*ess6(:,k) - ess3(:,k);

%-------------------------------------------------------------------%
% setpoint tracking

u_coi_set = ess1(:,k);                     % center setpoint

mask = (ess_con(:,3) ~= 0);                % Pade check
if any(mask)
    u_coi_set(mask) = theta_coi_pade(mask,k);
end
```

```
u_coi_err = u_coi_set - ess7(:,k);

mask = (u_coi_err < -ess_con(:,7));        % min rate limit
if any(mask)
    u_coi_set(mask) = ess7(mask,k) - ess_con(mask,7);
end

mask = (u_coi_err > ess_con(:,7));         % max rate limit
if any(mask)
    u_coi_set(mask) = ess7(mask,k) + ess_con(mask,7);
end

dess7(:,k) = (u_coi_set - ess7(:,k))./max(ess_con(:,8),lbnd);

mask = (ess_con(:,8) < lbnd);
if any(mask)                               % integrator bypass
    dess7(mask,k) = 0.0;
    ess7(mask,k) = u_coi_set(mask);        % center setpoint
end

u_local_set = ess2(:,k);                   % local setpoint

mask = (ess_con(:,3) ~= 0);                % Pade check
if any(mask)
    u_local_set(mask) = theta_ess_pade(mask,k);
end

u_local_err = u_local_set - ess8(:,k);

mask = (u_local_err < -ess_con(:,9));      % min rate limit
if any(mask)
    u_local_set(mask) = ess8(mask,k) - ess_con(mask,9);
end

mask = (u_local_err > ess_con(:,9));       % min rate limit
if any(mask)
    u_local_set(mask) = ess8(mask,k) + ess_con(mask,9);
end

dess8(:,k) = (u_local_set - ess8(:,k))./max(ess_con(:,10),lbnd);

mask = (ess_con(:,10) < lbnd);
if any(mask)                               % integrator bypass
```

```
    dess8(mask,k) = 0.0;
    ess8(mask,k) = u_local_set(mask);      % local angle setpoint
end

%-------------------------------------------------------------------%
% local LTV compensation path (alpha 1)

theta_err(:,k) = ess2(:,k) - ess1(:,k);

mask = (ess_con(:,3) ~= 0);                % Pade check
if any(mask)
    theta_err(mask,k) = theta_ess_pade(mask,k)...
                          - theta_coi_pade(mask,k);
end

u_a1hp = ess8(:,k) - ess7(:,k) - theta_err(:,k);

dess9(:,k) = ess_con(:,12).*u_a1hp
               - ess_con(:,14).*ess9(:,k) + ess10(:,k);
dess10(:,k) = ess_con(:,13).*u_a1hp
                - ess_con(:,15).*ess9(:,k);

u_a1c1 = ess_con(:,11).*(u_a1hp + ess9(:,k));

dess11(:,k) = (u_a1c1 - ess11(:,k))./max(ess_con(:,17),lbnd);

mask = (ess_con(:,17) < lbnd);
if any(mask)                               % integrator bypass
    dess11(mask,k) = 0.0;
    ess11(mask,k) = u_a1c1(mask);          % lead-lag state
end

tmp_a1c1 = ess11(:,k).*(1 - ess_con(:,16)./max(ess_con(:,17),lbnd));
u_a1c2 = tmp_a1c1 ...
          + u_a1c1.*(ess_con(:,16)./max(ess_con(:,17),lbnd));

dess12(:,k) = (u_a1c2 - ess12(:,k))./max(ess_con(:,19),lbnd);

mask = (ess_con(:,19) < lbnd);
if any(mask)                               % integrator bypass
    dess12(mask,k) = 0.0;
    ess12(mask,k) = u_a1c2(mask);          % lead-lag state
end
```

```
tmp_a1c2 = ess12(:,k).*(1 - ess_con(:,18)./max(ess_con(:,19),lbnd));
y_a1c2 = tmp_a1c2 ...
          + u_a1c2.*(ess_con(:,18)./max(ess_con(:,19),lbnd));

y_a1 = max(y_a1c2, ess_con(:,20));
y_a1 = min(y_a1, ess_con(:,21));

%-----------------------------------------------------------------%
% center LTI compensation path (alpha 2)

u_a2hp = ess7(:,k) - ess1(:,k);

mask = (ess_con(:,3) ~= 0);               % Pade check
if any(mask)
    u_a2hp(mask) = ess7(mask,k) - theta_coi_pade(mask,k);
end

dess13(:,k) = ess_con(:,23).*u_a2hp ...
                - ess_con(:,25).*ess13(:,k) + ess14(:,k);
dess14(:,k) = ess_con(:,24).*u_a2hp ...
                - ess_con(:,26).*ess13(:,k);

u_a2c1 = ess_con(:,22).*(u_a2hp + ess13(:,k));

dess15(:,k) = (u_a2c1 - ess15(:,k))./max(ess_con(:,28),lbnd);

mask = (ess_con(:,28) < lbnd);
if any(mask)                              % integrator bypass
    dess15(mask,k) = 0.0;
    ess15(mask,k) = u_a2c1(mask);         % lead-lag state
end

tmp_a2c1 = ess15(:,k).*(1 - ess_con(:,27)./max(ess_con(:,28),lbnd));
u_a2c2 = tmp_a2c1 ...
         + u_a2c1.*(ess_con(:,27)./max(ess_con(:,28),lbnd));

dess16(:,k) = (u_a2c2 - ess16(:,k))./max(ess_con(:,30),lbnd);

mask = (ess_con(:,30) < lbnd);
if any(mask)                              % integrator bypass
    dess16(mask,k) = 0.0;
    ess16(mask,k) = u_a2c2(mask);         % lead-lag state
end
```

```
tmp_a2c2 = ess16(:,k).*(1 - ess_con(:,29)./max(ess_con(:,30),lbnd));
y_a2c2 = tmp_a2c2 ...
          + u_a2c2.*(ess_con(:,29)./max(ess_con(:,30),lbnd));

y_a2 = max(y_a2c2, ess_con(:,31));
y_a2 = min(y_a2, ess_con(:,32));

%-----------------------------------------------------------------%
% computing the ess control command

u_lp = ess_con(:,33).*(y_a1 + y_a2);

dess17(:,k) = (u_lp - ess17(:,k))./max(ess_con(:,34),lbnd);

mask = (ess_con(:,34) < lbnd);
if any(mask)                                % integrator bypass
    dess17(mask,k) = 0.0;
    ess17(mask,k) = u_lp(mask);             % lowpass state
end

tmp_pcmd = max(ess17(:,k), ess_con(:,35));
ess_pcmd(:,k) = min(tmp_pcmd, ess_con(:,36));

%-----------------------------------------------------------------%
% converter interface

p_ord = ess_pcmd(:,k) ...
         + ess_con(:,39) + ess_sig(:,k) + ess_dsig(:,k);

p_ord_lb = -ess_pot(:,1);
p_ord_ub = ess_pot(:,1);

mask = (ess_soc(:,max(1,k-1)) <= ess_con(:,41));
if any(mask)
    p_ord_ub(mask) = 0.0;                   % discharging soc limit
end

mask = (ess_soc(:,max(1,k-1)) >= ess_con(:,42));
if any(mask)
    p_ord_lb(mask) = 0.0;                   % charging soc limit
end

mask = (ess_con(:,45) == 1);                % charge only mode
if any(mask)
```

```
    p_ord_ub(mask) = 0.0;
end

mask = (ess_con(:,45) == 2);               % discharge only mode
if any(mask)
    p_ord_lb(mask) = 0.0;
end

p_ord = max(p_ord, p_ord_lb);              % power limits
p_ord = min(p_ord, p_ord_ub);

%-------------------------------------------------------------------%
% real and reactive current saturation logic

u_ip_ord = ess3(:,k);                      % local voltage meas.

mask = (ess_con(:,3) ~= 0);                % Pade check
if any(mask)
    u_ip_ord(mask) = ess_vmag_pade(mask,k);
end

ess_ip_ord(:,k) = p_ord./max(u_ip_ord,lbnd);
ip_ord = ess_ip_ord(:,k);

mask = (ip_ord > ess_pot(:,1)./max(u_ip_ord,v_break));
if any(mask)
    ip_ord(mask) = ess_pot(mask,1) ...
                   ./max(u_ip_ord(mask),v_break(mask));
end

mask = (ip_ord < -ess_pot(:,1)./max(u_ip_ord,v_break));
if any(mask)
    ip_ord(mask) = -ess_pot(mask,1) ...
                   ./max(u_ip_ord(mask),v_break(mask));
end

ip_err = ip_ord - ess18(:,k);

mask = (ip_err < -ess_con(:,43));          % min rate limit
if any(mask)
    ip_ord(mask) = ess18(mask,k) - ess_con(mask,43);
end

mask = (ip_err > ess_con(:,43));           % min rate limit
```

```
        if any(mask)
            ip_ord(mask) = ess18(mask,k) + ess_con(mask,43);
        end

        dess18(:,k) = (ip_ord - ess18(:,k))./max(ess_con(:,44),lbnd);

        mask = (ess_con(:,44) < lbnd);
        if any(mask)                                % integrator bypass
            dess18(mask,k) = 0.0;
            ess18(mask,k) = ip_ord(mask);
        end

        ip_inj = ess18(:,k);                        % active current inj.

        dess19(:,k) = 0.0;                          % reactive placeholder
        ess19(:,k) = 0.0;

      % iq_inj = ess19(:,k);                        % reactive current inj.

        %-----------------------------------------------------------------%
        % state of charge tracking

        p_inj = ess_vmag(:,k).*ip_inj;
        p_ch = -min(p_inj,0);
        p_dis = max(p_inj,0);

        tmp_ch = ess_con(:,46).*p_ch - p_dis./max(ess_con(:,46),lbnd);
        dess20(:,k) = ess_pot(:,2).*tmp_ch;
        ess_soc(:,k) = ess_soc(:,1) + ess20(:,k);  % state of charge

    end
end

if (flag == 4)  % current calculation for nc_load
    if (i ~= 0)
        estr = 'ESS: Current calculation for nc_load must be vectorized!';
        error(estr);
    else
        busnum = bus_int(ess_con(:,2));             % bus number vector

        mask = isnan(vnc_ess);
        if any(mask)
            estr = 'ESS: Undefined voltage during nc_load calc. at ';
            estr = [estr, 'bus %0.0f.\n'];
```

```
    error(estr, busnum(mask));
end

%-----------------------------------------------------------------%
% LVPL logic

tmp_ip = ess18(:,k);
tmp_iq = ess19(:,k);

a_slope = i_lvpl1./(v_break - v_zerox);
b_inter = -i_lvpl1.*v_zerox./(v_break - v_zerox);

ip_inj_ub = i_lvpl1;

mask = (abs(vnc_ess) < v_break);           % linear roll-off
if any(mask)
    ip_inj_ub(mask) = a_slope(mask).*abs(vnc_ess(mask)) ...
                        + b_inter(mask);
end

mask = (abs(vnc_ess) < v_zerox);           % zero after this point
if any(mask)
    ip_inj_ub(mask) = 0.0;
end

mask = (tmp_ip > ip_inj_ub);               % enforcing the bound
if any(mask)
    tmp_ip(mask) = ip_inj_ub(mask);
end

mask = (tmp_ip < -ip_inj_ub);              % symmetric limits
if any(mask)
    tmp_ip(mask) = -ip_inj_ub(mask);
end

%-----------------------------------------------%
% final apparent power limiting stage

mask = (tmp_ip > ess_pot(:,1)./abs(vnc_ess));
if any(mask)
    tmp_ip(mask) = ess_pot(mask,1)./abs(vnc_ess(mask));
end

mask = (tmp_ip < -ess_pot(:,1)./abs(vnc_ess));
```

```
            if any(mask)
                tmp_ip(mask) = -ess_pot(mask,1)./abs(vnc_ess(mask));
            end

            tmp_inj = tmp_ip + 1j*tmp_iq;

            ess_sinj(:,k) = abs(vnc_ess).*tmp_inj;     % complex power inj.
            tmp_smod = ess_sinj(:,k) - ess_sinj(:,1);  % complex power mod.
            ess_cur(:,k) = conj(tmp_smod./max(vnc_ess,lbnd));

        end
    end
end

end  % function end

% eof
```

```
function [ angle_jump ] = ess_unwrap( angle_jump_pre, flag )
% ESS_UNWRAP Unwraps time-domain angle signals
%     This is a simple auxiliary function that unwraps time-domain
%     error signals. It accepts one argument angle_jump_pre which is
%     an angle difference in radians between the present and previous
%     samples. The output is a corrected angle jump that accounts for
%     wrapping in the phasor domain.
%-------------------------------------------------------------------------%

loop_lim = 2e3;
angle_jump = angle_jump_pre;               % initial angle jump vector

if (flag ~= 1)
    count = 0;                             % unwrapping phase angles
    while any(angle_jump >= pi)
        mask = (angle_jump >= pi);
        angle_jump(mask) = angle_jump(mask) - 2*pi;

        count = count + 1;
        if (count > loop_lim)              % infinite loop protection
            break
        end
    end

    count = 0;
    while any(angle_jump <= -pi)
        mask = (angle_jump <= -pi);
        angle_jump(mask) = angle_jump(mask) + 2*pi;

        count = count + 1;
        if (count > loop_lim)              % infinite loop protection
            break
        end
    end
end  % function end

% eof
```

VITA

Ryan Elliott is a Ph.D. candidate in the Department of Electrical and Computer Engineering at the University of Washington. His research focuses on renewable energy integration, wide-area measurement systems, and power system operation and control. Prior to pursuing a Ph.D., he was with the Electric Power Systems Research Department at Sandia National Laboratories from 2012–2015. While at Sandia, he served on the WECC Renewable Energy Modeling Task Force, leading the development of the WECC model validation guideline for central-station PV plants. In 2017, he earned an R&D 100 Award for his contributions to a real-time damping control system using PMU feedback. Ryan received the B.S.E.E. and M.S.E.E degrees from the University of Washington in 2009 and 2012, respectively.